AD-A174 261

CALCULATED AND MEASURED BLADE STRUCTURAL RESPONSE ON A FULL-SCALE ROTOR

Jacques Esculier
Ingenieur de l'Armement
STPA, Departement Helicopteres
75996 Paris Armees
France

and

William G. Bousman
Research Scientist
U.S. Army Aeroflightdynamics Directorate
Moffett Field, California 94035-1099

DTIC
ELECTE
NOV 18 1986
S
D
A

Abstract

The restricted problem of the calculation of the bending-moment response of a full-scale rotor to measured airloads is studied here. Data are used from separate tests of an articulated rotor in flight and in a wind tunnel. Linear equations to represent the blade mass and structure are used, and the solution is obtained by numerically solving the resulting two-point boundary problem. The measured aerodynamic loads include effects caused by both rigid blade motion and elastic deformation, and, hence, represent an exact aerodynamic model. By comparing the calculated blade-bending and torsional-moment response with measurement, it is possible to assess the adequacy of the structural model for the calculation of vibratory loads. These comparisons are good for the flap- and torsional-moments at the lower harmonics. The calculations for the chord-bending moments are less satisfactory, and reveal problems with the method of deriving the chord airloads from the measured normal forces, or the representation of the nonlinear lead-lag damper. The good agreement that is seen for the flap- and torsional-moments represents a case of self-validation as the differential-pressure and strain-gage measurements are independent sets of measurements.

Notation

A	state matrix for flap and chord equations
B	state matrix for torsion equation
C	chord airload along airfoil chordline, lb/in.
C_T	rotor-thrust coefficient
C_1, C_2, C_3, D	flap and chord variables, Eq. (15)
c_ℓ	section-lift coefficient
E	Young's modulus, lb/in.^{2}
G	shear modulus, lb/in.^{2}
F_n	aerodynamic-force vector, lb
F_y	aerodynamic force in hub plane, lb
F_{ync}, F_{yns}	cosine, sine force components in hub plane, lb
F_z	aerodynamic force normal to the hub plane, lb
F_{znc}, F_{zns}	cosine, sine force components normal to the hub plane, lb
I_1, I_2	bending moments of inertia about major and minor axes respectively, in.^{4}
J	torsional-stiffness constant
k_m	polar radius of gyration of cross-sectional mass
k_{m1}, k_{m2}	mass radii of gyration about major and minor axes respectively
L	linear operator
M_n	aerodynamic pitching-moment vector, in.-lb
M_{nc}, M_{ns}	cosine, sine pitching-moment components, in.-lb
M_x	pitching moment, in.-lb
M_{xnc}, M_{xns}	cosine, sine torsional moments
M_{xn1}, M_{xn2}	phase-shifted torsional moments, Eq. (19)

DTIC FILE COPY

This document has been approved for public release and sale; its distribution is unlimited.

86 9 22 093

M_{y1n}, M_{y2n}	phase-shifted flap-bending moments, Eq. (13)
M_{ync}, M_{yns}	cosine, sine flap-bending moments
M_{z1n}, M_{z2n}	phase-shifted chord-bending moments
M_{znc}, M_{zns}	cosine, sine chord-bending moments
m	blade mass-per-unit length, slugs/in.
N	aerodynamic force normal to blade chord
n	harmonic
P	rotor thrust, lb
R	blade radius, in.
r	blade radial coordinate, in.
T	tensile force, lb
V	airspeed, knots
V_{y1n}, V_{y2n}	phase-shifted chord shears, lb
V_{ync}, V_{yns}	cosine, sine chord shears, lb
V_{z1n}, V_{z2n}	phase-shifted flap shears, lb
V_{znc}, V_{zns}	cosine, sine flap shears, lb
v	chord coordinate, in.
v_i	induced velocity, Eq. (8)
v_{io}	thrust-induced velocity, Eq. (9)
v_{nc}, v_{ns}	cosine, sine chord displacements, in.
w	flap coordinate, in.
w_{nc}, w_{ns}	cosine, sine-flap displacements, in.
X_n	state vector for flap and chord equations
x	chord displacement made dimensionless by blade chord
Y_n	state vector for torsion equation
α_s	shaft angle, deg
β	undeformed-blade pitch angle, rad
γ	blade structural damping (twice damping ratio)
γ_{nc}, γ_{ns}	cosine, sine slopes for chord equation, rad
γ_{1n}, γ_{2n}	phase-shifted slopes for chord equation, rad
Δp	differential pressure, $lb/in.^2$
ρ	air density, $slugs/ft^3$
σ	rotor solidity
ϕ	torsion coordinate, rad
ϕ_{nc}, ϕ_{ns}	cosine, sine-torsion displacement, rad
ψ	blade azimuth, deg
ψ_{nc}, ψ_{ns}	cosine, sine slope for flap equation, rad
ψ_{1n}, ψ_{2n}	phase-shifted slope for flap equation, Eq. (13), rad
Ω	blade rotational frequency, rad/sec and rpm
ω	frequency of vibration, rad/sec
$( )'$	d/dr

Introduction

The calculation of the loads on a rotor blade requires an accurate representation of the aerodynamic forces along the blade, and an accurate representation of the blade structure and mass properties. To calculate the fatigue loading of a new rotor-blade design, it is usually sufficient to accurately represent the loading caused by the steady, first, and second harmonic airloads. If it is necessary to calculate the vibratory loads, an accurate representation of the third, fourth, and fifth harmonic loads is required (for a four-bladed rotor). Ormiston has compared the predictions made by analysts in the helicopter industry for the loads on a hypothetical rotor.[1] This comparison demonstrated that reasonably good agreement was obtained for the prediction of the flapwise peak-to-peak loads, but the chordwise peak-to-peak loads were strongly affected by the damper model used in the calculation, and the agreement was not as good. The predictions of the torsional and vibratory loads did not show good agreement. Ormiston concluded that the

difficulties encountered were caused by weaknesses in the aerodynamic model, the structural model, and the solution methods, and recommended that efforts be made to achieve improvements in all of these areas.

The problem of calculating rotor loads is fundamentally an aeroelastic one, so it is not easy to separate the aerodynamic and structural models and examine them separately. One attractive approach is, however, to use the airloads measured in flight as a forcing function for the structural model of the rotor. The attractiveness of this approach is that the measured airloads include the loading caused by the undeformed rotor blade as well as the loads caused by the blade's aeroelastic response. A comparison of the calculated and measured response will then allow an assessment of the adequacy of the structural model. This is the problem addressed in this paper.

A similar approach has been taken with the full-scale rotor loads data obtained on the XH-51A compound helicopter.[2] In that case, the blade structure was represented by nonrotating modes, and the response was computed using the measured airloads. The calculated bending moments showed good agreement for flapping on the outboard section of the blade, and for the chord bending, but the flap-bending moments on the inner portion of the blade and the torsion moments did not show good agreement. The reasons for these difficulties were not clear.

The full-scale data on the XH-51A represent one set of data that is suitable for the calculations discussed here. Hooper has surveyed the full-scale rotor-loads data published in the literature which include both the measurements of the airloads on the blade and the blade's structural response.[3] Of the seven sets of data he described, two are for two-bladed configurations, two are for compound aircraft, and three are for conventional articulated rotorcraft. The data that have been selected for use in this paper are for the CH-34 rotor, both from the flight test[4] and the wind tunnel test.[5] This rotor is articulated in flap and chord, and has been designed to minimize the coupling between the blade's degrees of freedom. The resulting simplicity in the mathematical representation is desirable for the purposes of this paper. The paper will briefly review the flight- and wind tunnel test measurements, and discuss the mathematical representation of the blade. Comparisons between the calculated and measured trim values, and flap, chord, and torsional moments will be presented. Conclusions will be made as to the adequacy of the structural model and the validity of the measurements, and recommendations for future tests will be made.

Full-Scale Rotor Loads Measurements

Flight-Test Measurements

Flight-test measurements were made on a CH-34 helicopter rotor and reported in Reference 4. These measurements were made on a standard aircraft, except for the modifications needed to install differential pressure transducers and strain gages on the blades. The data were recorded on oscillograph rolls, and read into a computer using semiautomatic film-reading equipment. Data from three rotor revolutions or cycles were averaged for the flight cases discussed in this paper. The magnitude of errors in the recording and transcribing of the data was estimated in Reference 4, and varied depending upon the measurement, but generally fell within the limits of ±5%. No estimate was made of phase errors. Data were samples every 15° in azimuth, or 24 times per revolution, thus giving a bandwidth of 12 harmonics.

Twenty-two flight cases were selected from the 94 flight conditions reported in Reference 4. Eighteen of these cases were trimmed-level flight cases (or in a few cases with a slight rate of climb or descent) with the airspeed varying from approximately 0 to 122 knots. The remaining four cases were obtained in steady turns at load factors from 1.32 to 1.52 g. There was significant variation in rotor speed between the various flight cases with values ranging from 190 to 246 rpm. For each flight case, the time histories of the differential pressures, the flap-bending moments, the chord-bending moments, the torsional moments, and the pitch-horn loads were combined with the harmonics of the blade-root motions to create a database. Normal force and aerodynamic pitching moment were obtained from the tabulated differential-pressure data by integrating the functions $\sqrt{\bar{x}}\Delta p$ and $(0.25 - x)\sqrt{\bar{x}}\Delta p$ as a function of $\sqrt{\bar{x}}$ using a trapezoidal integration.

Wind Tunnel Measurements

Wind tunnel measurements were obtained with a CH-34 rotor and reported in Reference 5. The rotor was mounted on a standard CH-34 transmission and driven by a 1500-horsepower, variable-speed electric motor. The transmission was supported on an I-beam framework within an aerodynamic fairing, and mounted to the wind tunnel balance. The control system was redesigned to increase the strength of the controls for the higher loads anticipated in the wind tunnel tests, and to minimize pitch-lag coupling. The swashplate actuators from the CH-34 aircraft were replaced with S-61 actuators to handle the increased loads. As a result of these modifications, pairs of adjacent blades had slightly different cyclic pitch angles,

and there was a split of the tip-path plane of about an inch between adjacent pairs. The instrumented blade and its preceding blade constituted one pair so the major influence of the preceding blade's vortex was not affected by the tip-path plane split. The rotor blades were standard CH-34 blades except for the modifications made to the instrumented blade to install the pressure transducers.

The data were multiplexed and recorded on FM tape. Ten revolutions, or cycles, of data were obtained for each condition, and the data were sampled 72 times per revolution and averaged. In this way, time histories of the data were obtained with an azimuth spacing of 5°, thus providing a bandwidth of 36 harmonics. Using this processing scheme, there was no evidence of amplitude or phase distortion out to the twentieth harmonic. An estimate of the static error gave values of 2.2% of full scale for the strain gages, and 4.1% of full scale for the blade pressures.

All ten of the wind tunnel cases reported in Reference 5 were used for this study. The tunnel speed ranged from 110 to 175 knots and the shaft angle varied from +5° to -9°. Except for one full-lift case at 110 knots, the rotor was unloaded for these tests to about 60 or 70% of the normal thrust. All test conditions were run with a rotor speed of 222 rpm. Time histories of the differential pressures for these tests were obtained from Reference 6, and these histories were combined with the time histories of the measured flap, chord, torsional stresses, and the harmonics of the blade root motions to create the database used here. Normal force and pitching moment were obtained from the tabulated differential pressure data in the same manner as discussed for the flight-test data. To allow comparison between the bending-moment data of flight and wind tunnel tests, the latter were converted from blade stress to bending moment using the stress-moduli values reported in Reference 7.

Comparison of Flight and Wind Tunnel Tests

The differences between the flight and the wind tunnel tests of the CH-34 rotor are in some cases important when using the data. The basic differences fall into the following categories: 1) rotor configuration, 2) vehicle configuration, 3) test measurements, 4) data reduction, and 5) test conditions. In general, the rotor configuration was identical for both flight and wind tunnel tests. As a result of the redesigned rotating controls for the wind tunnel test, there was a tip-path plane split of about an inch between adjacent pairs of blades.

In terms of vehicle configuration, the major difference between the two tests were the differences in impedance of the hub and control system, and the aerodynamic flow field. In neither case was the impedance at the hub or the control system measured, and the effect on the data is not quantified. The aerodynamic flow-field differences in the two tests are primarily the result of differences between the aircraft fuselage and the faired body used in the wind tunnel. Some small differences caused by the wind tunnel wall effects are also expected.

The measurements made in the two sets of tests were not identical. In the case of the differential pressures, additional pressure transducers were added at the span stations of 0.97R and 0.99R for the wind tunnel test as indicated in Table 1. The selection of bending-moment bridge locations was different between the two tests as is shown in Table 2. In the flight test, ten harmonics of the blade-root motion were tabulated. However, in the wind tunnel test, only the steady and first harmonic motions were given for the pitch and lag motions, and only four harmonics of flapping. The only measure of rotor power in the flight test was the engine manifold pressure, which was considered unreliable. In the wind tunnel, rotor power was determined directly from

Table 1. Quantity of Differential Pressure Transducers

Test	Radial location								
	0.25R	0.40R	0.55R	0.75R	0.85R	0.90R	0.95R	0.97R	0.99R
Flight	5	5	7	7	11	7	7	0	0
Wind tunnel	5	5	7	7	11	7	7	4	3

Table 2. Bending-Moment, Strain-Gage Bridge Location

Test	Radial location								
	0.150R	0.275R	0.375R	0.450R	0.500R	0.575R	0.650R	0.800R	0.825R	0.925R
Flight	F,C,T	F	F,C	F	T	F,C	F	F*	C*	F*
Wind tunnel	C,T		F,C,T	F			F,C,T	F,C		

*Obtained for 4 of 22 cases.

shaft-mounted strain gages. The flight test measured the pitch-link load, but this was not done in the wind tunnel.

The major difference in the data-reduction procedures was the use of oscillograph data and the semiautomation of the digitizing process for the flight test, compared to the FM multiplex recording used for the wind tunnel test. Error estimates made by the respective investigators suggest that both the static and dynamic errors were higher for the flight test, but the numbers are not directly comparable. The wind tunnel data were averaged over ten cycles, or rotor revolutions, and some sample results show that there was very little scatter from cycle to cycle. The flight-test data were averaged over three cycles, and it is not clear how repeatable the data were. For most of the cases in the wind tunnel, the data were reported with a bandwidth of 36 harmonics, compared to the 12 harmonic bandwidth of the flight test, but for the study of the vibratory loads in the area of 3, 4, and 5 harmonics, it does not appear that this difference is important.

A significant difference between the two tests was the range of test conditions. This is shown in Fig. 1, where the 22 flight, and the 10 wind tunnel test conditions are shown on a plot of the rotor-lift coefficient, C_T/σ, as a function of advance ratio. Data obtained from a model test of a CH-47 rotor are shown on this plot to indicate the steady-lift limit on a rotor independent of structural considerations.[8] The flight-test data were obtained for a variety of lift coefficients up to an advance ratio of about 0.30. The wind tunnel data were obtained for advance ratios of 0.30 and above, and there is only a slight zone of overlap. The scatter in the value of the lift coefficient for the flight-test data is due to

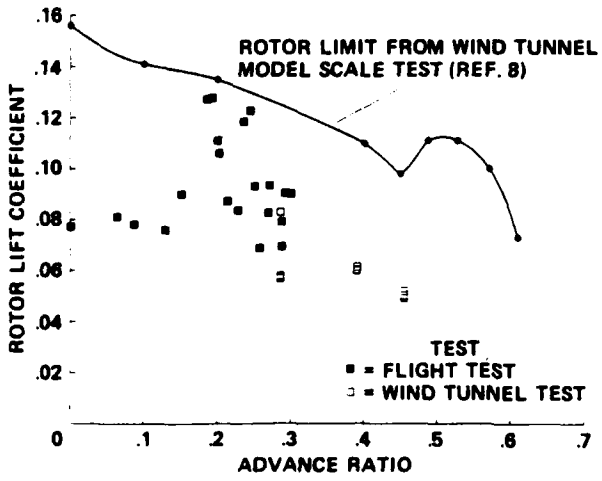

Figure 1. CH-34 full-scale test data.

differences in the rotor speed between flight conditions. The four rotor-lift coefficient values that are closest to the aerodynamic lift boundary are from the steady-turn flight conditions, but in general, the other flight and wind tunnel conditions are well separated from the aerodynamic lift limit.

Example of Measured Airloads and Bending Moments

Examples of the data obtained from the CH-34 rotor tests are shown in Figs. 2 and 3 in the manner of Hooper.[3] Each figure shows the measured parameter in a Cartesian coordinate system plotted as a function of the rotor azimuth and the blade radial location. The figures on the left show the measured results for the full range of harmonics while the figures on the right show only the harmonics above 2/rev, that is, the harmonics that are important for vibration for a four-bladed rotor. Figure 2 shows the measured normal force, and the flap- and chord-bending moment response. The airloads include harmonics up to the 36th; however, for this case the bending moment data in Reference 5 were given only for the first 10 harmonics. From the figure of the normal force it can be seen that the blade is highly loaded at the 0° azimuth, and as the blade comes around, the lift is reduced and even becomes negative near 90°. The lift again becomes positive and shifts inboard as the azimuth increases and shifts outboard as the blade returns to 0°. The flap-bending moment is dominated by a 2/rev loading on the front and rear sides of the disk. The chord-bending moment shows a strong 1/rev loading for these same conditions. The steady chord bending is not included in this last figure because an examination of the data has shown that it depends only upon rotor speed, and is caused by the effects of small offsets between the mass center and tensile axis. In the case of the vibratory loading, the impulsive or doublet airload discussed by Hooper in Reference 3 occurs near an azimuth angle of 90°. It appears that the blade responds to this excitation at 3/rev, which is to be expected considering that the second flap mode is calculated to be at about 2.7/rev. The chord-bending moment response is a mixture of 3 and 4/rev which is again expected as the second-chord mode is calculated to be at about 3.5/rev.

The measured, aerodynamic pitching moment, obtained from an integration of the differential pressures, and the torsional moment are shown for the same case in Fig. 3. The pitching-moment data show two major features. First, there is a large, positive spike on the outer portion of the blade at an azimutgh of 90°. The pitching moment then goes negative at a slightly higher blade azimuth and closer to the blade tip. The effect of this change from a positive to negative pitching moment

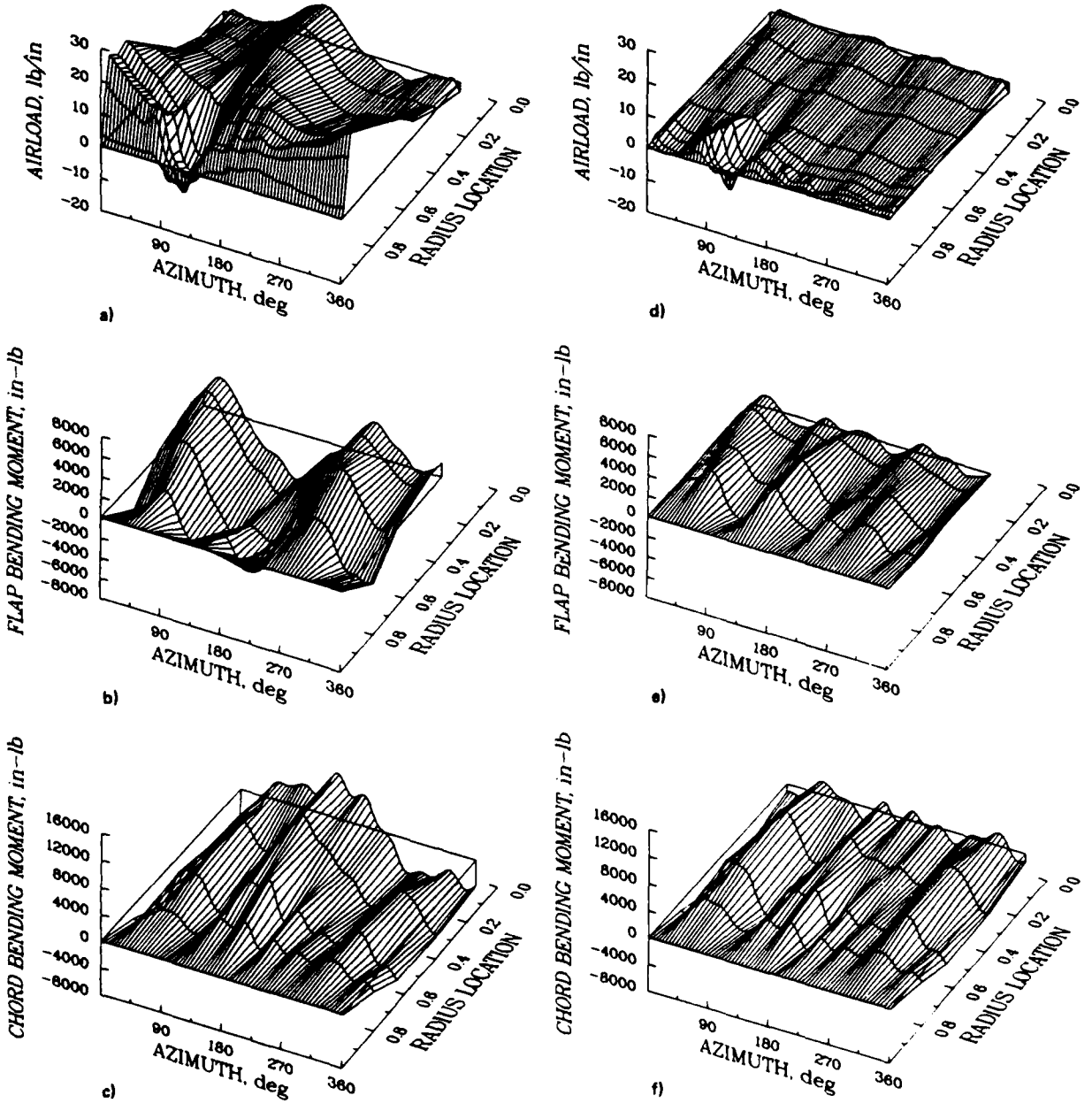

Figure 2. Cartesian plots of CH-34 wind tunnel normal force and bending-moment data; V = 150 knots, shaft angle = -5°. a) Normal force; 0-36 harmonics. b) Flap-bending moment; 0-10 harmonics. c) Chord-bending moment; 1-10 harmonics. d) Normal force; 3-36 harmonics. e) Flap-bending moment; 3-10 harmonics. f) Chord-bending moment; 3-10 harmonics.

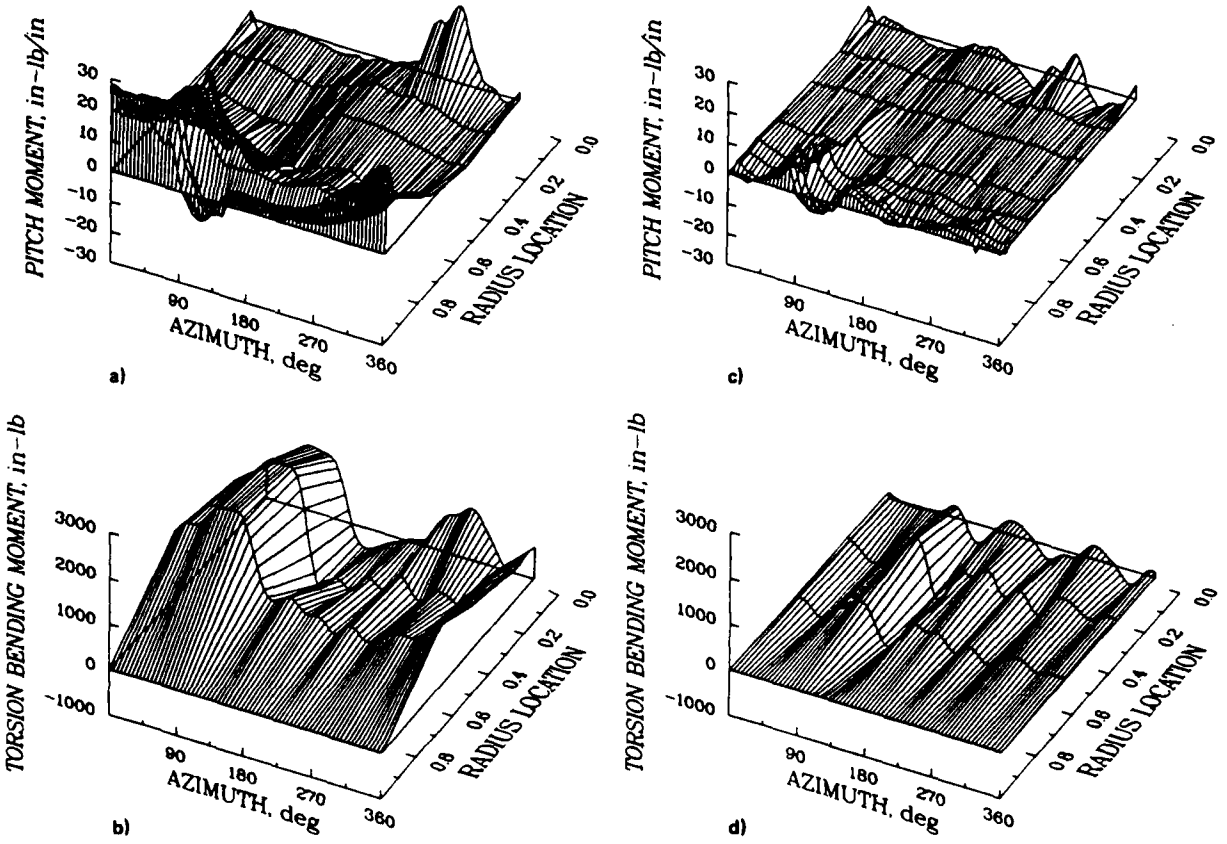

Figure 3. Cartesian plots of CH-34 wind tunnel pitching moment and torsional-moment data; V = 150 knots, shaft angle = -5°. a) Pitching moment; 0-36 harmonics. b) Torsional moment; 0-10 harmonics. c) Pitching moment; 3-36 harmonics. d) Torsional moment; 3-10 harmonics.

is evident in the torsion bending-moment measurements which show a rapid reduction in bending moment at all three measurement stations. The second feature in the pitching-moment data is another positive loading that occurs at the inboard measurement location at about 270°. This is the effect of reverse flow on the rotor. The effect is large because the force acts over a moment arm of half a blade chord. The torsional-moment data also show this effect for the inboard measurement station. The plots of the vibratory data show that the impulsive load that was seen in the normal force data is also seen in the pitching-moment data. The response in the torsional moment is a combination of many harmonics.

Calculation Method

Linear Equations

The blade is considered to be a beam whose behavior can be represented by a set of three linear, partial differential equations for the flap, chord, and torsion degrees of freedom. For the calculations made here, the equations derived in Reference 9 have been used. These equations are coupled by the blade's geometric pitch angle; the offsets between the tensile, mass, elastic, and feathering axes; and the cross-section integrals defined in Reference 9. In the case of the CH-34, the blade has been designed to minimize the various offsets and, where these offsets have been estimated, the values are zero or close to zero. For this paper, the axis offsets and cross-section integrals have been set to zero, and this results in the flap and chord equations being coupled only by the local pitch angle and a separate, uncoupled torsion equation. The resulting equations are

$$[(EI_1 \cos^2 \theta + EI_2 \sin^2 \theta)w'' + (EI_2 - EI_1)\sin \theta \cos \theta v'']'' - (Tw')' + m \frac{\partial^2 w}{\partial t^2} = F_z \qquad (1)$$

$$[(EI_2 - EI_1)\sin\beta\cos\beta w'' + (EI_1\sin^2\beta + EI_2\cos^2\beta)v'']'' - (Tv')' + m\frac{\partial^2 v}{\partial t^2} - \Omega^2 mv = F_y \quad (2)$$

$$(-GJ\phi')' + \Omega^2 m[(k_{m2}^2 - k_{m1}^2)\phi + mk_m^2\frac{\partial^2\phi}{\partial t^2} = M_x \quad (3)$$

The left-hand sides of these equations represent the structural and mass properties of the blade, whereas the right-hand side is the aerodynamic force on the blade. Limited calculations have been made with a fully coupled set of equations that include the axis offsets and cross-section integrals, but the effect of these additional terms is slight. The actual values of these small coupling terms are also difficult to estimate from available rotor documentation.

Solution Process

The partial differential equations that represent the blade's response to the aerodynamic forces are reduced to a set of ordinary differential equations by writing the variables and forces as terms in a Fourier series, and solving for each harmonic separately. Each of the differential equations is therefore transformed to $2n + 1$ equations, where n is the number of harmonics that are used in the solution. The individual equations are reduced to a set of first-order linear equations using the approach of Reference 10 of the form

$$X_n' = AX_n + F_n \quad (4)$$

For each harmonic, then, the system of differential equations may be solved as a two-point, boundary value problem. The flap equation is assumed to have zero displacement, zero moment at the root of the blade, and zero moment at the tip. For the chord equation the displacement at the root, and the moment at the tip are also assumed to be zero, but the moment at the root depends upon the representation of the blade damper. For the torsion equation either the displacement at the root is specified as a function of swashplate motion or the moment at the root is specified as a function of pitch-link load. In either case, the moment at the tip is zero.

The sine and cosine harmonics of the solution are coupled through the structural damping. As the equations of motion may be written in terms of a linear operator

$$L(x) + m\frac{\partial^2 x}{\partial t^2} = F \quad (5)$$

Then the structural damping may be added as a velocity term in the equation[14]

$$L(x) + \frac{\gamma}{\Omega}L\left(\frac{\partial x}{\partial t}\right) + m\frac{\partial^2 x}{\partial t^2} = F \quad (6)$$

and the sine and cosine harmonics will be coupled by the damping term. The final form of Eq. (4) is given in the appendix.

Derivation of Chord Airloads

The integration of the differential pressure measurements on the rotor blade provides a direct measure of the aerodynamic normal force and the pitching moment acting on the blade. There is no direct measure of the chord force, however, so it is necessary to derive this force using two-dimensional, airfoil section data. These section data may be used to determine the chord force as indicated in the schematic of Fig. 4. If the normal force is known, by then calculating the velocity it is straightforward to enter two-dimensional tables, and derive the force that is parallel to the airfoil chord line. Data for the NACA 0012 airfoil have been conveniently arranged in this form, in Reference 2, to give the dimensionless chord force as a function of the dimensionless normal force and Mach number. This set of curves has been used for all the calculations shown in this paper. Once the chord force in the airfoil plane is determined the forces in the hub plane axes are calculated

$$F_z = N$$
$$F_y = N\sin\beta + C\cos\beta \quad (7)$$

The calculation of the chord force requires the measured normal force and the calculated velocity at the airfoil section. The calculated

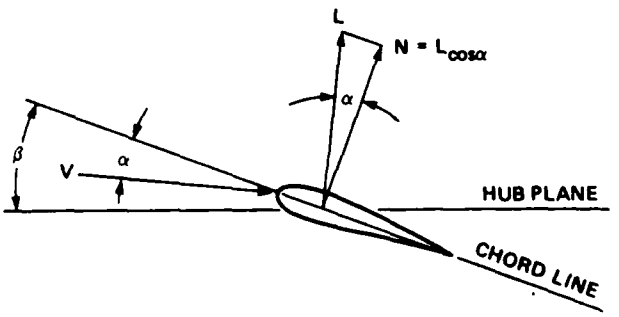

Figure 4. Orientation of forces on airfoil.

velocity is dependent upon inplane components caused by forward speed and rotation, and out-of-plane components caused by the induced flow, shaft tilt, coning, and first-harmonic flapping. The model used for the induced flow is a simple representation that includes the effects of a fore-to-aft variation in induced flow over the rotor disk.[12]

$$v_i = v_{io}\left\{1 + r\cos\psi \tan\left[\frac{1}{2}\tan^{-1}\left(\frac{V\cos\alpha}{v_{io}}\right)\right]\right\} \quad (8)$$

where

$$v_{io} = \frac{P}{2\pi V\rho R} \quad (9)$$

The values used for shaft tilt, coning, flapping, and lift are taken from the flight or wind tunnel measurements. Near the reversed flow region, the velocity tends to a very low number and calculated c_ℓ calues can become quite large. In these areas the section lift coefficient is arbitrarily limited to 3. No attempt has been made to include either the effects of elastic flapping or torsional motion in the calculation, or the influence of pitch-rate or acceleration on the forces involved.

The calculated chord airloads are shown in Fig. 5 for the 150-knot wind tunnel case with the shaft angle at -5°. The doublet airloading that is prominent in the normal force and pitching moment is also seen in Fig. 5. There is also a strong 1/rev variation that provides an airfoil thrusting force in the first quadrant, and a drag force in the third quadrant. This effect is primarily the result of cyclic pitch variation and its effect on the normal-force component of the chord airload.

Calculation Process

The steps that are used in the calculation process to obtain the rotor response from the measured airloads are:

1) The normal force and pitching-moment airloads are obtained for each solution point along the blade radius using linear interpolation from the data.

2) Chord forces are derived for each radial station where the normal force was measured by calculating the velocity for that blade station and using that velocity to calculate the normal force coefficient. The airfoil section data from Reference 2 are then used to obtain the force coefficient parallel to the airfoil chord line, and these data are resolved to the hub plane of the rotor. The chord force for each solution point is obtained by linear interpolation from the derived chord forces.

3) The centrifugal loads are calculated every inch along the blade using the mass properties for the CH-34 rotor published in Reference 7.

4) The equations of motion are solved using the program DVCPR,[13] which is a two-point, boundary-value problem solver. Structural and mass properties for the blade are taken from Reference 7. An uncoupled solution of the flap and chord equations is obtained with the blade pitch angle set to zero (in which case the equations are uncoupled), or a coupled solution is obtained with the pitch angle determined at each blade station as a function of the collective and cyclic pitch angles at the blade root, and the built-in twist angle.

5) The solution values for slope, moment, and shear are phase-shifted to account for the structural damping.

6) For the uncoupled solution, the calculations are left in the hub-plane axes, whereas for

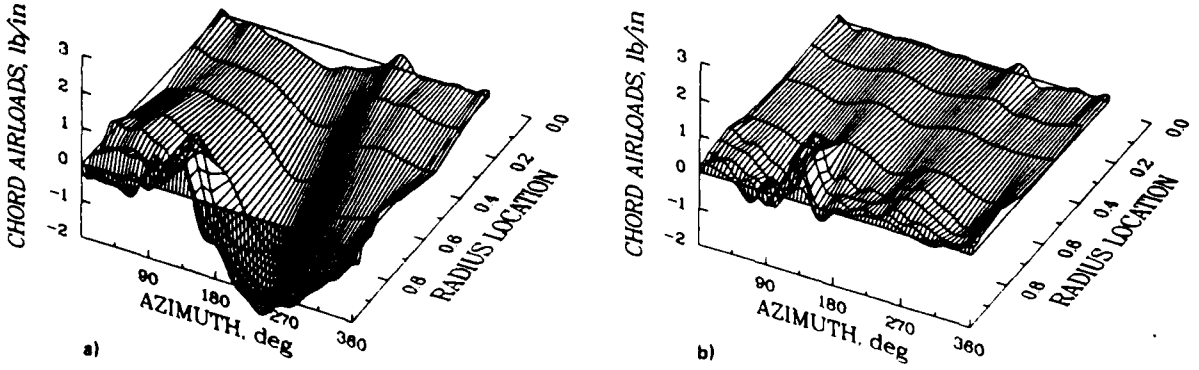

Figure 5. Chord airloads derived from measured normal force; drag on airfoil is a negative load. a) 0-10 harmonics. b) 3-10 harmonics.

the coupled solution, the calculations are transformed to the local blade axes using the blade pitch angle.

The two-point boundary value equation solver, DVCPR, is given the maximum number of grid points it may use in the solution. A maximum grid size of 200 points was used for the results shown in this paper. A few cases were run for larger grid sizes, and the effects of grid size were determined. For a grid size of 350, the change in calculated bending moments was of the order of 0.5%. However, neither the slopes nor the shears achieved this accuracy; for example, the difference in the blade root angles and shears for grid sizes of 200 and 350 points was of the order of 5%.

Results

Blade Natural Frequencies

The blade-mode natural frequencies were calculated in vacuum using the equations of Reference 9, and the structural properties for the CH-34 rotor obtained from Reference 7. The results of these calculations are shown in Fig. 6,

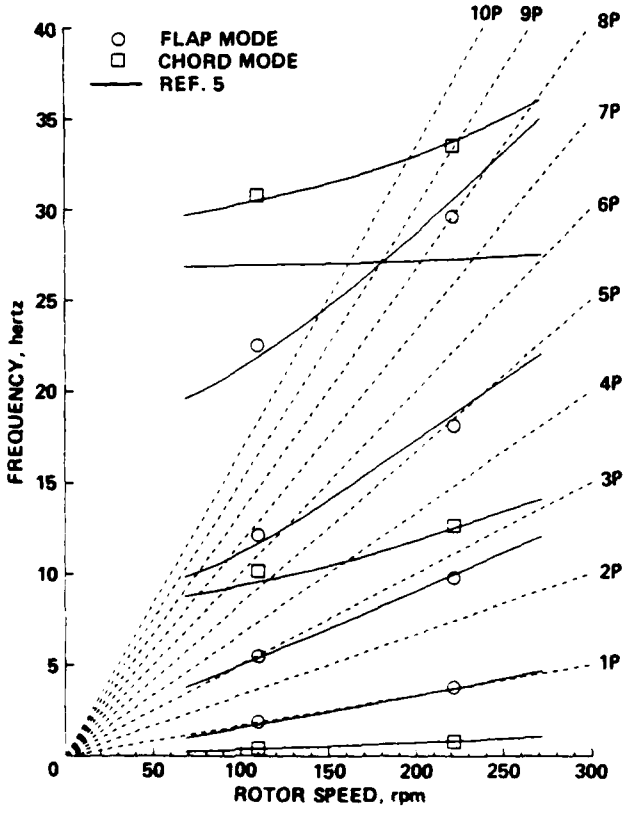

Figure 6. CH-34 rotor predicted natural frequencies.

which plots the rotating-system natural frequencies as a function of rotor speed. The predictions shown with the lines are the natural-frequency calculations reported in Reference 5. The symbols are the calculation made in the present study. In general, the agreement between the two sets of calculations is good. Unfortunately, there are no structural test data that can be used to verify these calculations.

Rotor Trim

The solution of the flap and chord equations provides the displacement, slope, bending moment, and shear at each grid point along the blade. The rotor thrust and power can be calculated from the shears at the blade hinges, and can be compared with the aircraft weight for the flight tests, or with the lift and power measured in the wind tunnel. The calculated blade angles at the hinge point can be compared directly with the measured values. Because of the wide variety of flight- and wind tunnel test conditions, the calculations and measurements were compared by plotting the calculated values as a function of the measurements. Table 3 shows the mean difference between the calculation and measurement, and the correlation coefficient for rotor lift and power. The correlation coefficient provides an estimate of how well the calculation and measurement agree, whereas the mean difference defines the average offset. For the flight test, the mean difference of the calculated lift less the measured lift was -416 lb, or -3.0%. This comparison is only approximate, however, as the aircraft weight was not reported for the individual flights. For the results shown here, a median weight of 11,500 lb is used, which is midway between the reported range of flight-test weights of 11,200 to 11,805 lb. The measurement of engine power was not considered accurate for the flight test,[4] so it is not considered here.

For the wind tunnel test, the calculated lift averaged 137 lb or 1.9% high, with a range of values from -4.1 to 11.3%. For the power, the calculated value was 182 hp low. This difference was consistent over a range of conditions from propulsive force to autorotation, and for tunnel speeds from 110 to 175 knots. This relatively constant difference suggests that the estimate of the profile power is too low, and this may be related to limitations in the derivation of the chord airloads.

The mean differences and correlation coefficients for the comparison of the calculated and measured trim angles are shown in Table 4. The calculated and measured coning are well correlated for both the flight and wind tunnel tests. For the flight test, the calculated coning averages 0.86° higher than the measurements; this is not

NTIS GRA&I
DTIC TAB
Unannounced
Justification
By
Distribution/
Availability Codes
Dist Avail and/or Special
A-1

Table 3. Mean Differences and Correlation Coefficients for Rotor Lift and Power

Test	Lift, lb		Power, hp	
	diff	r	diff	r
Flight	-416	0.958	--	--
Wind tunnel	137	0.960	-182	0.993

Table 4. Mean Differences and Correlation Coefficients for Rotor Trim Angles

Trim angle	Test	Steady, deg		Longitudinal, deg		Lateral, deg	
		diff	r	diff	r	diff	r
Flapping	Flight	0.86	0.905	-0.55	0.334	1.12	0.128
Flapping	Wing tunnel	0.20	0.927	0.56	0.347	4.43	0.223
Lead-lag	Flight	0.39	0.738	-0.13	0.702	-0.06	0.777
Lead-lag	Wind tunnel	2.55	0.987	-0.40	-0.552	-0.11	0.725

consistent with the comparison for lift in which the calculated lift averaged lower than the estimated vehicle weight. The reason for these differences is unknown. The wind tunnel test calculated coning averages 0.20° or 6.8% high. The steady lag angles of the flight-test data show a lot of scatter in their values, and this is reflected in the poor correlation coefficient. As with the case for rotor power, the steady lag-angle comparison for the wind tunnel data shows a difference that is consistent over all of the wind tunnel conditions, and suggests the blade-profile power has been underestimated.

The first-harmonic trim angles show considerable scatter as is indicated by the correlation coefficients in Table 4. The comparison of the first-harmonic flapping angles is shown in Fig. 7a. The flight-test data, which are shown with the solid symbols, show a calculated range from -4.3 to 2.9° whereas the measurements show an excursion of only -1.0 to 0.6°. The correlation between measurement and calculation is poor. The same situation is also seen for the wind tunnel data, although here the range of measured flapping angles is greatly increased. It is not clear why the differences between the calculation and measurement occur. It is possible that the calculated flapping angles are extremely sensitive to

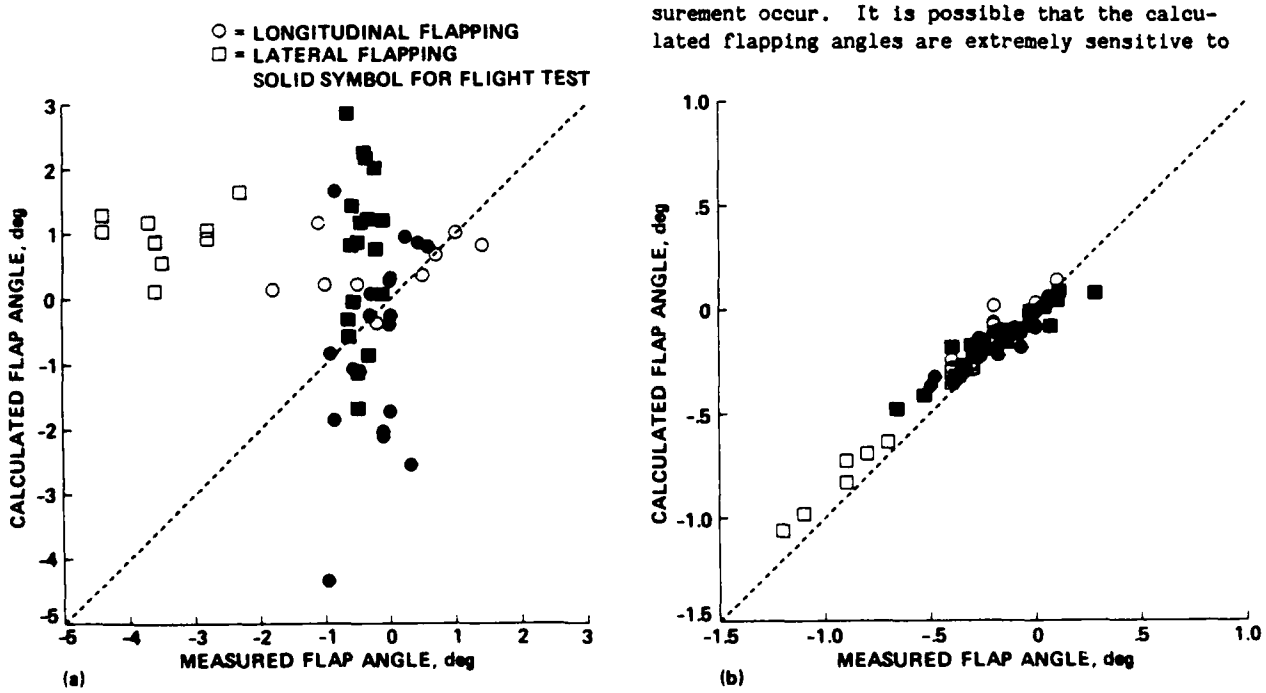

Figure 7. Comparison of calculated and measured blade-flapping angles. a) First harmonic flapping. b) Second harmonic flapping.

the measured airloads for the first harmonic solutions because the system's natural frequency is so close to 1/rev. In this respect it is interesting to note that the agreement between calculation and measurement is very good for the second harmonic flapping as shown in Fig. 7b. This suggests that the calculation of the flapping angles is accurate away from 1/rev. The sensitivity of the flapping angles to the airloads was also observed in Reference 5 in which sample calculations were made of the airloads using the measured trim and calculations made using trim angles of 0°. The effect of a change in the lateral trim from -4.4 to 0° was to change the calculated airloads at the blade tip by 10 to 20%, thus any error in measurement of the airloads at the blade tip could affect the calculation of the flapping trim.

Flap-Bending Moment

Comparison with Wind Tunnel Data. The results of the uncoupled calculation for the flap-bending moment are compared to the data in Fig. 8 for the 150 knot, -5° shaft angle case. The upper pair of figures shows the loading for 0-10 harmonics and the lower pair shows the vibratory loading for 3-10 harmonics. As discussed previously the 0-10 harmonic loads are dominated by the 2/rev loading, whereas the vibratory loads are the result of the 2nd flap bending mode being slightly below 3/rev. The agreement between the calculations and measurements is excellent, with nearly identical details seen in terms of both amplitude and phase.

This agreement can be examined more closely by comparing the calculations and measurements along the blade span for each harmonic individually as is shown in Fig. 9. In this figure, the amplitude scale is allowed to vary for each harmonic so the details of the comparison may be observed even when the harmonic component is very small. The measurements are shown as the solid symbols and both the coupled and uncoupled calculations are shown. The agreement is very good, particularly for the lower harmonics. For the

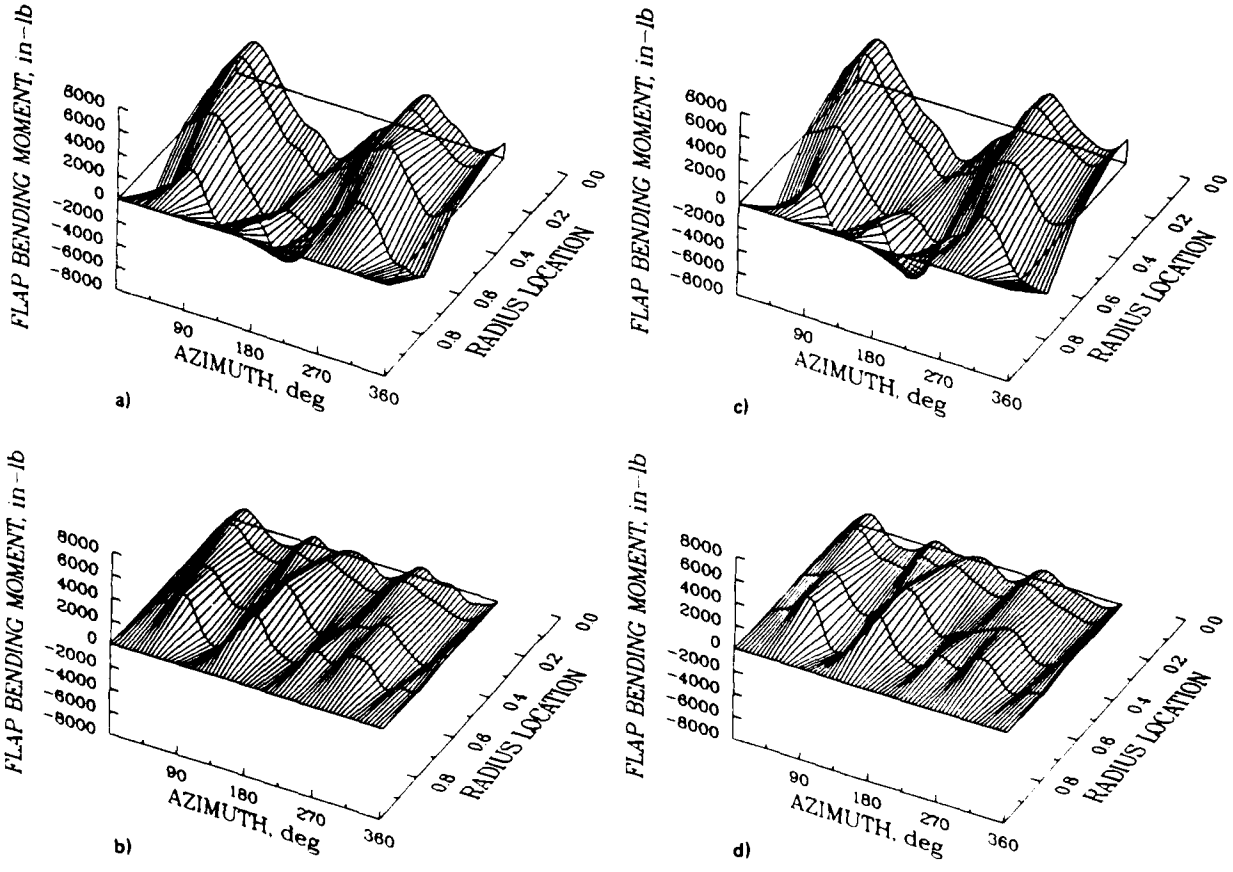

Figure 8. Calculated and measured flap-bending moments; wind tunnel, V = 150 knots, shaft angle = -5°. a) Measured flap-bending moment, 0-10 harmonics. b) Measured flap-bending moment, 3-10 harmonics. c) Calculated flap-bending moment, 0-10 harmonics. d) Calculated flap-bending moment, 3-10 harmonics.

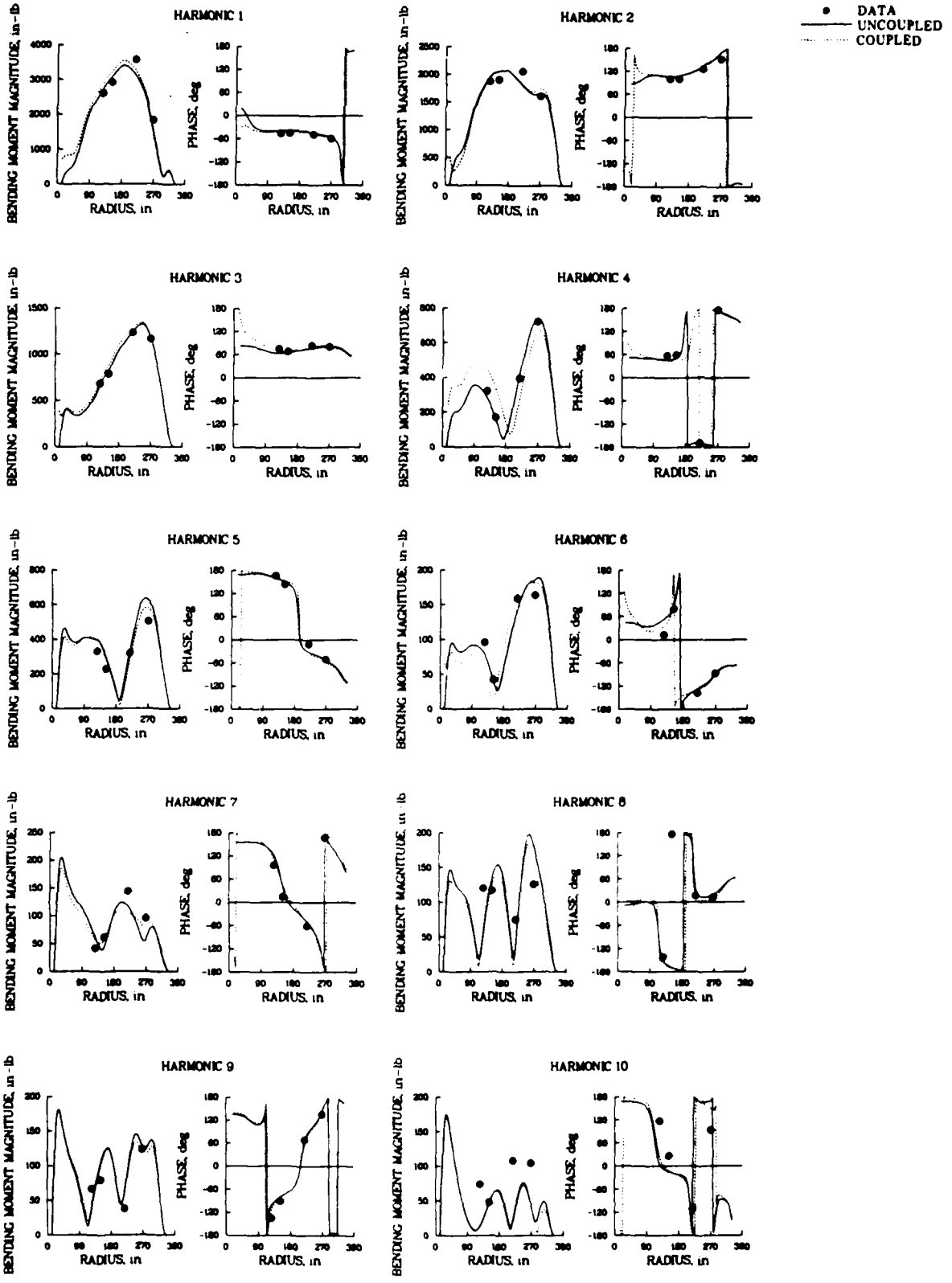

Figure 9. Harmonics of flap-bending moment as a function of radius; wind tunnel, V = 150 knots, shaft angle = -5°.

higher harmonics, the higher bending modes become more important, and it is more difficult to make judgments based on only four measurement points. Despite this difficulty, the amplitude values, and especially the phase, look very good up through the 9th harmonic.

The case shown in Fig. 9 is typical of the results obtained for the flap-bending moment in the wind tunnel, with the exception of the 5th and 8th harmonics, which, for most of the other wind tunnel cases, do not show good agreement in the bending moment amplitude. For those cases, the calculated 5th and 8th harmonics are approximately twice the measured values. As can be seen in Fig. 6, the 3rd and 4th flap-bending modes are predicted to be very close to 5/rev and 8/rev. If the actual bending modes are further from the per rev resonance condition than the prediction, then a reduction in the moment would be expected. Additional evidence that the calculated loads are being strongly affected by the 3rd and 4th flap-bending modes were obtained by repeating the calculation with the structural damping reduced from 2% to 0. The only harmonics affected were the 5th and 8th which showed a 30 to 50% increase in amplitude.

In general, the effect of coupling with the chord degree of freedom shows only a minor effect on the flap-bending moments. As expected, when the degrees of freedom are coupled, the flap-bending moment no longer goes to zero at the blade hinge because of the damper force in the chord degree of freedom. In a few cases, better agreement with the data is seen with the coupled calculation as opposed to the uncoupled calculation, but there is no consistent trend one way or the other.

A curious feature that is seen in the 1st-harmonic bending moment is the variation in bending that occurs near the blade tip. This can be more easily understood if the results are shown as the cosine and sine solution rather than amplitude and phase. In Fig. 10, both the sine and cosine solutions show a reversal in bending that occurs near the blade tip. For the cosine solution the blade is above the hub plane, and in the vicinity of the blade tip the centrifugal and inertial forces cause the blade to bend down. As the lift becomes effective moving inboard from the tip, the moment reverses and becomes positive. The reversals in bending moment in the cosine and sine solutions combine in amplitude, and cause the variation in bending noted.

Comparison with Flight-Test Data. The comparison of the calculated and measured, flap-bending moments for a flight-test case at 112 knots and 216 rpm (Flight 18) is shown in

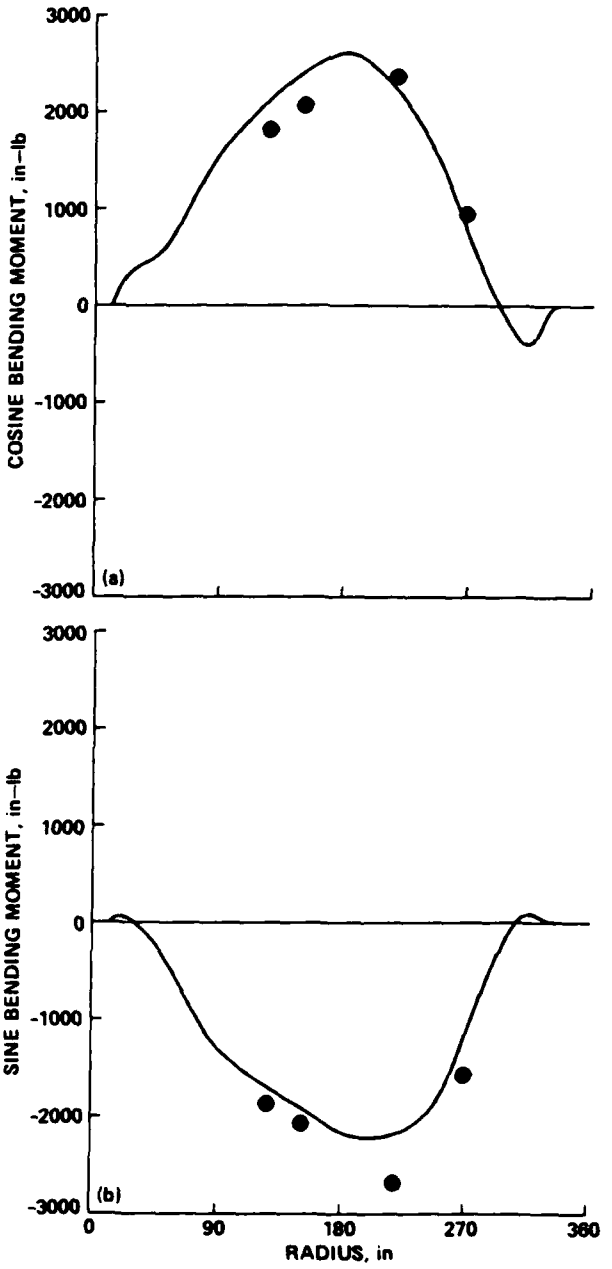

Figure 10. First harmonic flap-bending moment as a function of radius; wind tunnel, V = 150 knots, shaft angle = -5°. a) Cosine bending moment. b) Sine bending moment.

Fig. 11. As with the wind tunnel case, the bending-moment loads are dominated by the 2/rev loading in forward flight, while the vibratory loads are affected primarily by the 2nd flap-bending moment near 3/rev. The agreement shown in Fig. 11 is good; however, a careful examination shows some differences, and these are more easily seen in the

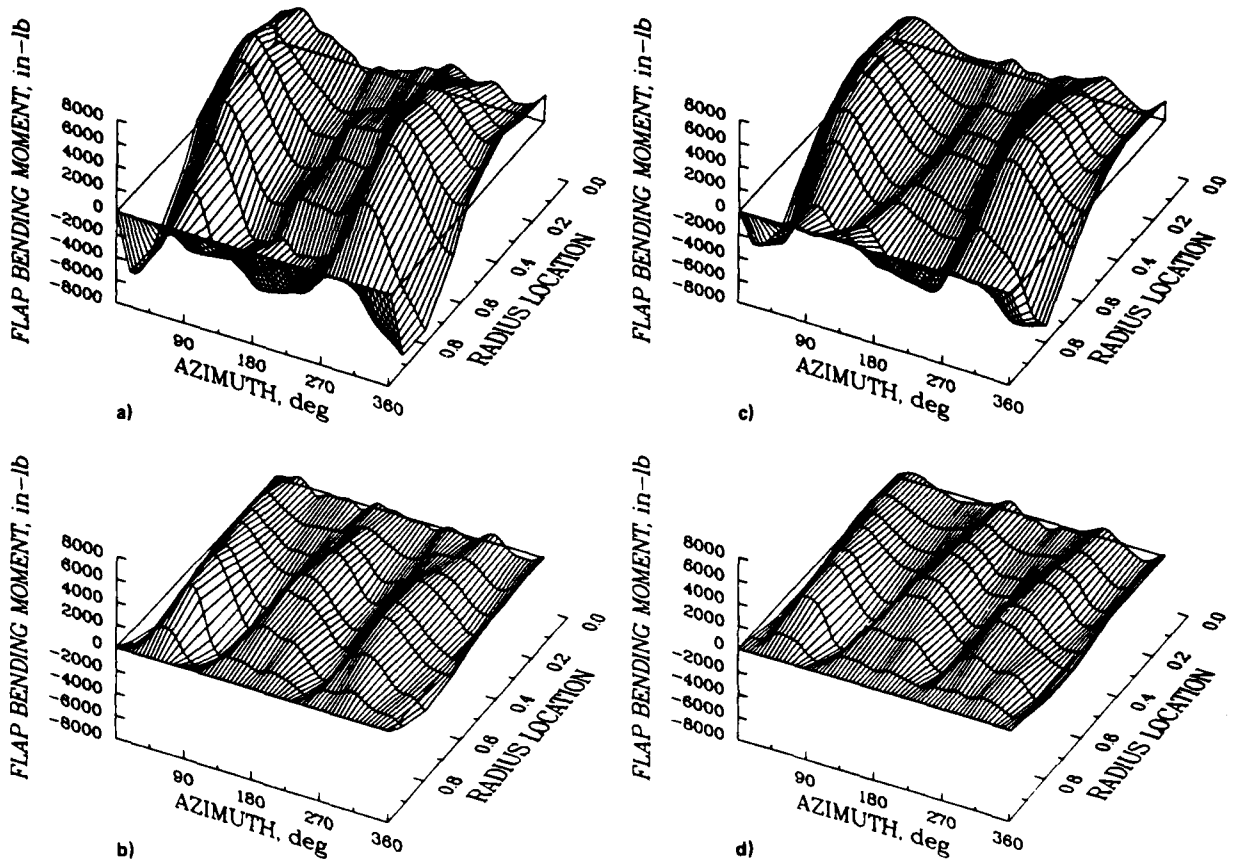

Figure 11. Calculated and measured flap-bending moments; flight test, V = 112 knots, rotor speed = 216 rpm. a) Measured flap-bending moment, 0-12 harmonics. b) Measured flap-bending moment, 3-12 harmonics. c) Calculated flap-bending moment, 0-12 harmonics. d) Calculated flap-bending moment, 3-12 harmonics.

detailed comparison shown in Fig. 12. The behavior for this case is much like the wind tunnel case, at least up to the 6th harmonic. In general, the agreement between the calculations and the measurements is quite good up to the 5th harmonic. Beyond the 5th harmonic, the results are not consistent, and there are substantial differences in both amplitude and phase. The effects of these differences were not noticeable in the Fig. 11 comparison because the load levels are so small.

Comparisons have been made between the calculations and measurements for the other flight test cases and, in general, there is good agreement for the first three harmonics of blade flap bending. For the 4th through 6th harmonics the amplitude results are variable, but the phase results are generally good. Above the 6th harmonic, the results are highly variable, and there is no consistent behavior that is identifiable.

Adequacy of Calculation of Flap-Bending Moments. The comparison of the calculated and measured flap-bending moments for the wind tunnel and flight tests shows very good agreement for the lower harmonics of rotor loads. This is particularly true for the wind tunnel tests. This indicates that with a correct aerodynamic model, there should be no major difficulty in accurately calculating the flap-bending moments and shears as long as the blade structural properties are known.

The comparison of calculation and measurement for the wind tunnel data shows good agreement up to the 9th harmonic. For the flight-test data, the comparison starts to degrade beyond the 3rd or 4th harmonic and even at the lower harmonics the calculation tends to be lower than the measurement at midspan. Sample calculations were made with the wind tunnel data, removing the two outer spanwise airload measurement stations, so as to simulate the flight-test measurement configuration.

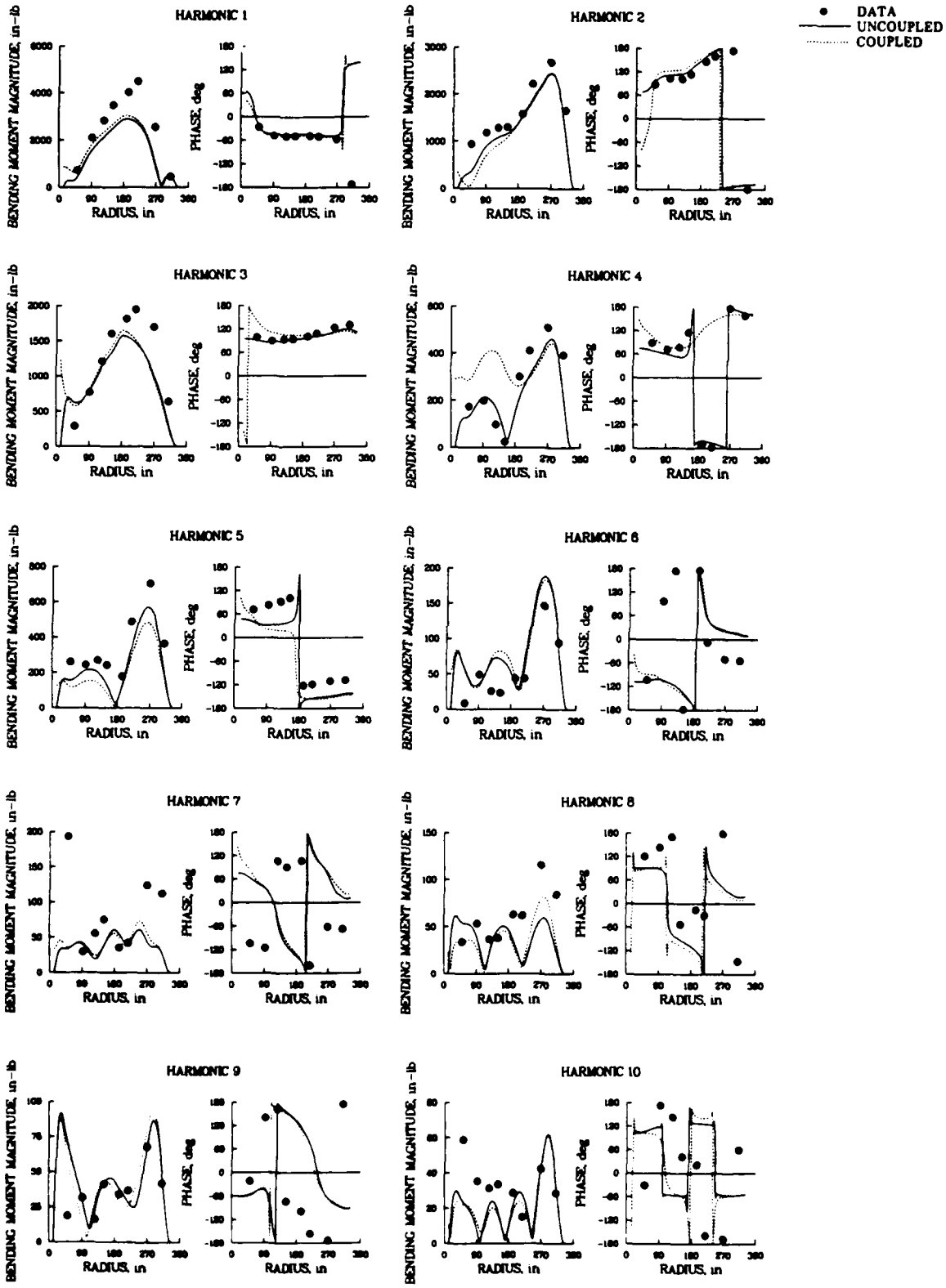

Figure 12. Harmonics of flap-bending moment as a function of radius; flight test, V = 112 knots, rotor speed = 216 rpm.

The effect on the calculated flap bending moment was minor, and no harmonic load was affected more than any other. Other differences between the wind tunnel and flight test that may relate to the poorer agreement observed in the higher harmonics of the flight-test data include: 1) the steadiness or unsteadiness of the rotor trim condition, 2) the difference in the number of cycles used in averaging the data, 3) the process of digitization from oscillograph records used for the flight-test data, and 4) differences in hub impedance between the wind tunnel and flight test.

The good agreement that is seen between the calculation and measurement for the wind tunnel test provides a measure of validation of both the differential pressure measurements and the strain-gage data. As the two sets of measurements are independent, the agreement shown here is a case of mutual validation and demonstrates there are no significant errors in either set of measurements.

Some ambiguities remain in interpreting the differences between the calculations and measurements. For the wind tunnel test, differences were seen in the 5th and 8th harmonic that were ascribed to the effects of the 3rd and 4th flap-bending modes. It is important in future flight, or wind tunnel tests on a rotor with comparable instrumentation, that structural shake tests of the blade be performed to identify the nonrotating modal frequencies. During the test program, rotor-speed sweeps should be made to identify the rotating modal frequencies of those modes that are proximate to per rev lines and to characterize the load variation with rotor speed. In addition, the impedance of the test aircraft or stand should be determined. The use of strain-gage information requires that the grid of strain gages be at least as fine as the grid of pressure transducers.

Chord-Bending Moment

Comparison with Wind Tunnel Data. The calculation of the chord-bending moment using the coupled equations is compared with the measurements in Fig. 13 for the 150 knot, -5° shaft angle

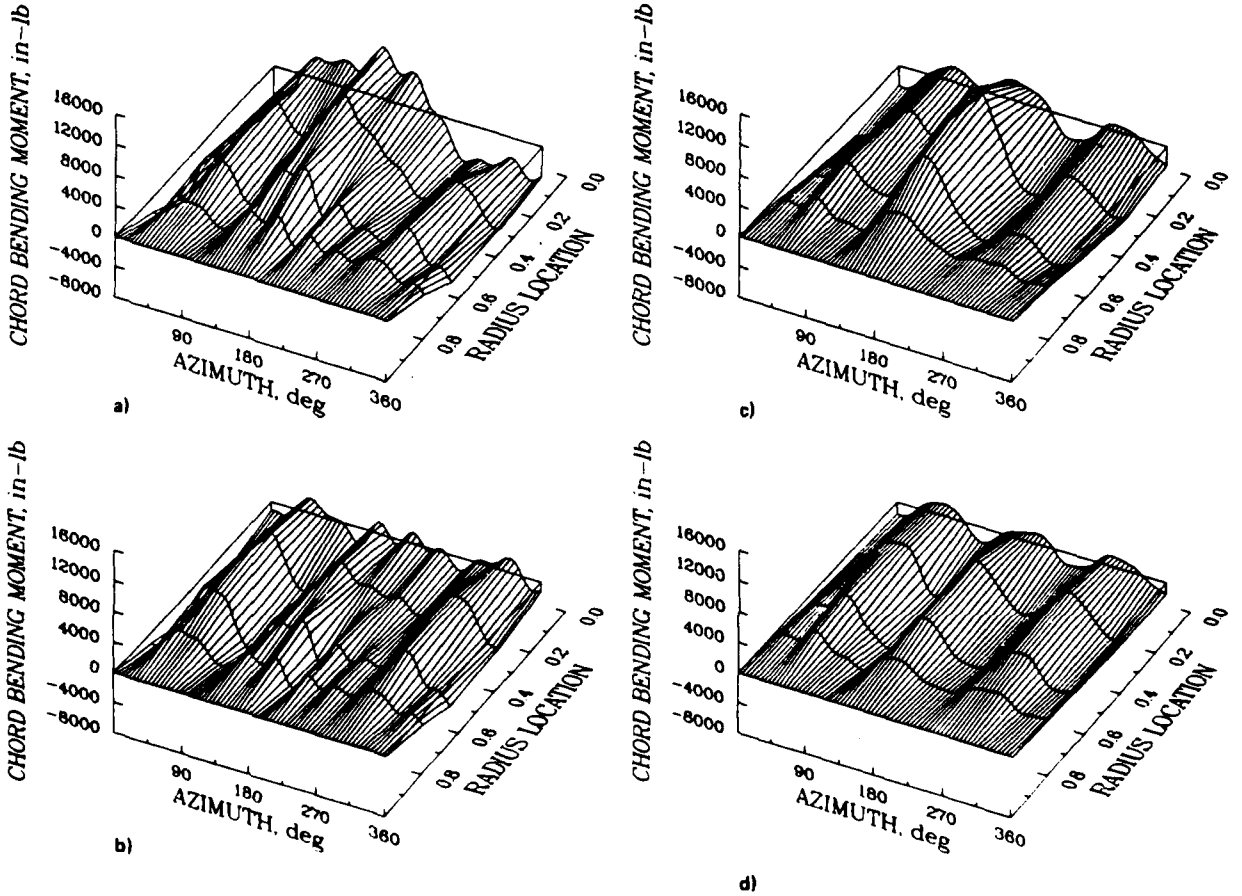

Figure 13. Calculated and measured chord-bending moments; wind tunnel test, V = 150 knots, shaft angle = -5°. a) Measured chord-bending moment, 1-10 harmonics. b) Measured chord-bending moment, 3-10 harmonics. c) Calculated chord-bending moment, 1-10 harmonics. d) Calculated chord-bending moment, 3-10 harmonics.

case. The upper pair of figures shows the overall loading and the lower pair the vibratory loads. Unlike the comparisons for the flap-bending moment, substantial differences between the calculated and measured, chord-bending moments are seen. The measurements show a large 1/rev component that increases from blade tip to root, large 3/rev loading, and a good bit of higher harmonic loading which is largely a result of the 3rd chord-bending mode in the vicinity of 8 and 9/rev. The calculations show the basic 3/rev character which is caused by the 2nd chord-bending mode, but exhibit neither the 1/rev or higher harmonic loadings.

A detailed comparison of the calculations and measurements for each harmonic is shown in Fig. 14. For the 1st harmonic component, the measured load continually increases from the blade tip to the blade root, but the coupled calculation shows an initial increase, and then a decrease and reversal in the bending moment. The amplitude of the 2nd harmonic is low, relative to the 1st harmonic, and the calculated and measured bending moments show similar amplitudes, but the phase agreement is not good. The linear model of the blade does not allow for the nonlinear terms that result from the Coriolis forces, so good agreement may be difficult to achieve for this harmonic. The 3rd harmonic shows good agreement between the coupled calculation and the measurement, both in amplitude and phase. The calculation for the 4th harmonic is substantially below the measurement, and the phase is incorrect. The higher harmonics are of low amplitude with respect to the 3/rev loading, and have only a minor effect upon the chord-bending moments. An exception is the 8th harmonic which shows relatively large, measured loads that are a result of the proximity of the 3rd chord-bending mode. The theoretical prediction of the 3rd chord-bending mode shows that it should occur near 9/rev, but even allowing for the difference in the frequency of the calculated and measured 3rd chord-bending modes it is clear that the measured response for this mode is considerably greater than the calculation. The results shown here for the 150 knot, -5° shaft-angle case are typical for all of the wind tunnel conditions.

In comparing the calculation and measurements for the flap-bending moments, it was shown that the coupling between the flap and chord degrees of freedom was not important in calculating the loading. The same result is not expected for the calculation of the chord-bending moments since the forces in the flap direction are very much larger than the forces in the chord direction and, therefore, the effect of coupling through the local blade pitch angle should result in substantial blade-bending moments. That this is the case is also shown in Fig. 14 where the coupling terms of the flap- and chord-bending equations have been set to zero, and the loading is caused only by the derived chord airloads. In general, the calculated chord-bending moments using the uncoupled equations are substantially lower than the calculation using the coupled equations, and are also substantially below the measurements. In particular, the phase angle that is obtained using the uncoupled calculation is significantly in error in nearly all cases.

It is unclear how important the derived chord airloads are to the calculation of the chord-bending moments, as compared to the effects of coupling with the flap degree of freedom, and the normal airloads. One way of looking at this problem is to solve the flap and chord equations with the chord force, F_y, set to zero. This is also shown in Fig. 14, and, as can be seen, there is an improvement in the agreement of the calculation and measurements for the 1st harmonic (except at the most inboard station), but for the other harmonics, the results are largely the same.

Comparison with Flight-Test Data. The calculation using the coupled equations and the measurements are compared in Fig. 15 for the same flight-test case shown in Fig. 11. As with the wind tunnel data, the measurements are dominated by 1/rev and 3/rev loads. The calculation does not properly represent the 1st harmonic loads, but does show fairly good agreement for the vibratory loads.

A detailed comparison of the calculations and measurements for the individual harmonics is shown in Fig. 16. The results of the comparison are very similar to the wind tunnel case in Fig. 14. The 1st harmonic loading is poorly estimated using the coupled equations, while the 3rd harmonic shows good agreement between the measurements and calculations. The 4th harmonic is substantially underpredicted. The poor representation of the 4th harmonic loads is seen consistently in both the wind tunnel and flight-test data. This discrepancy is interesting because any vibratory coupling with the drive train would appear at 4/rev, 8/rev, and so forth. In the presence of drive train coupling, the assumption that the blade root is undergoing only steady rotation would be incorrect. Agreement between the calculation and measurements for the higher harmonics is generally poor. It is interesting to note that the flight-test data do not show a strong loading at 8/rev because of the 3rd chord-bending mode. As with the wind tunnel data, the calculation using the uncoupled equations is unable to represent the bending moments measured on the blade and shows large phase errors. If the solution is made with the chord force set to zero, then some improvement is seen in the 1st harmonic loads, but there is generally little difference between using the coupled equations with or without the chord airloads.

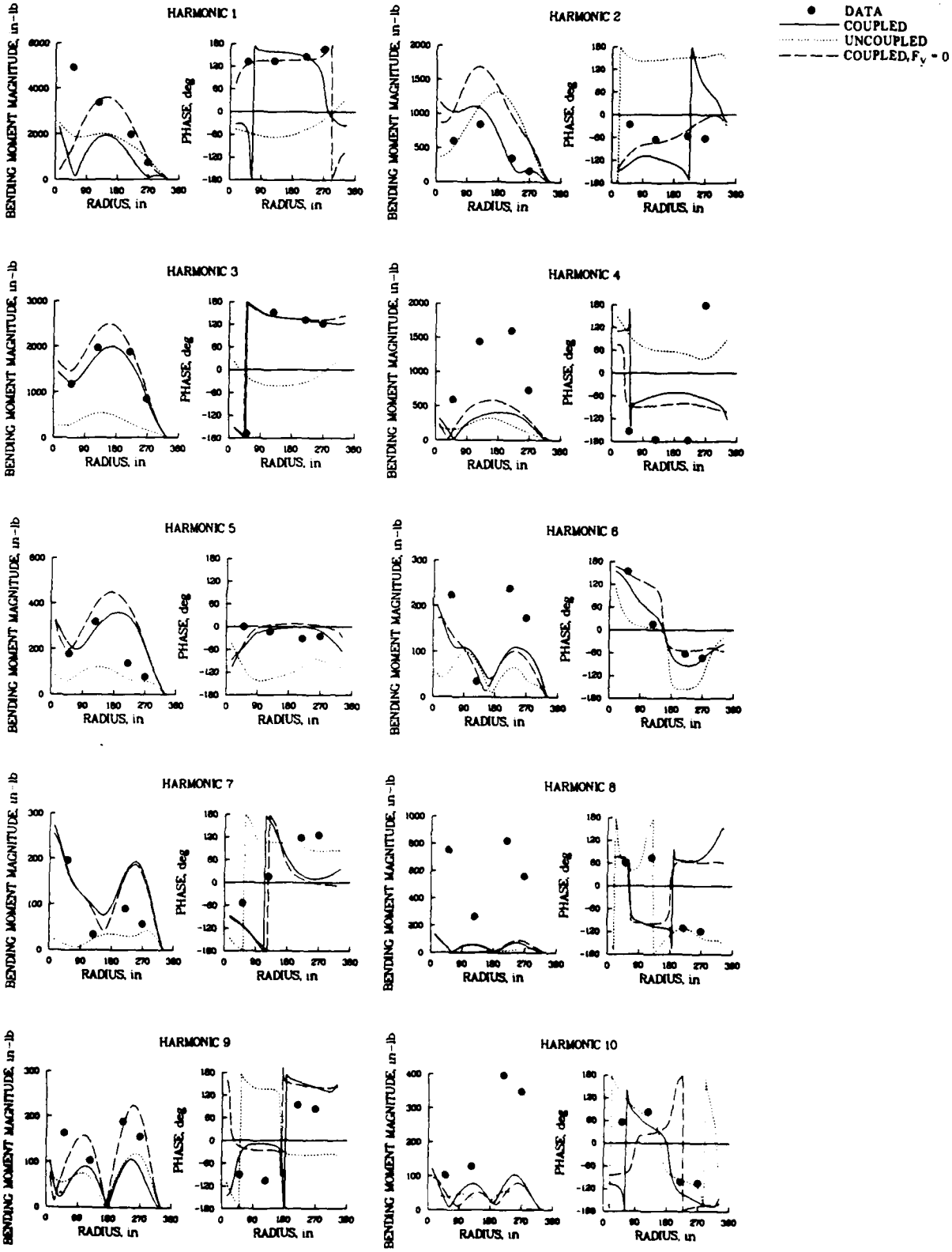

Figure 14. Harmonics of chord-bending moment as a function of radius; wind tunnel test, V = 150 knots, shaft angle = -5°.

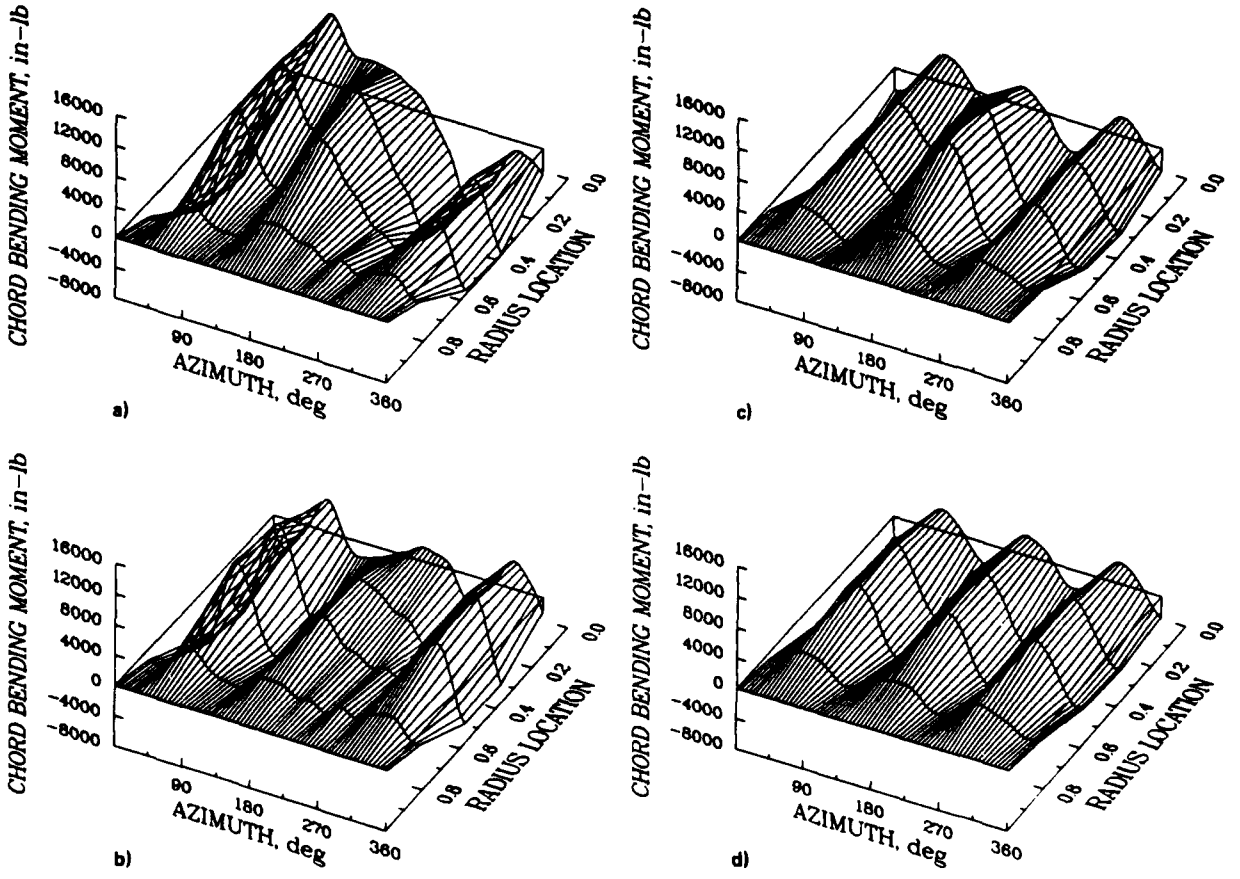

Figure 15. Calculated and measured chord bending moments; flight test, V = 112 knots, rotor speed = 216 rpm. a) Measured chord-bending moment, 1-10 harmonics. b) Measured chord-bending moment, 3-10 harmonics. c) Calculated chord-bending moment, 1-10 harmonics. d) Calculated chord-bending moment, 3-10 harmonics.

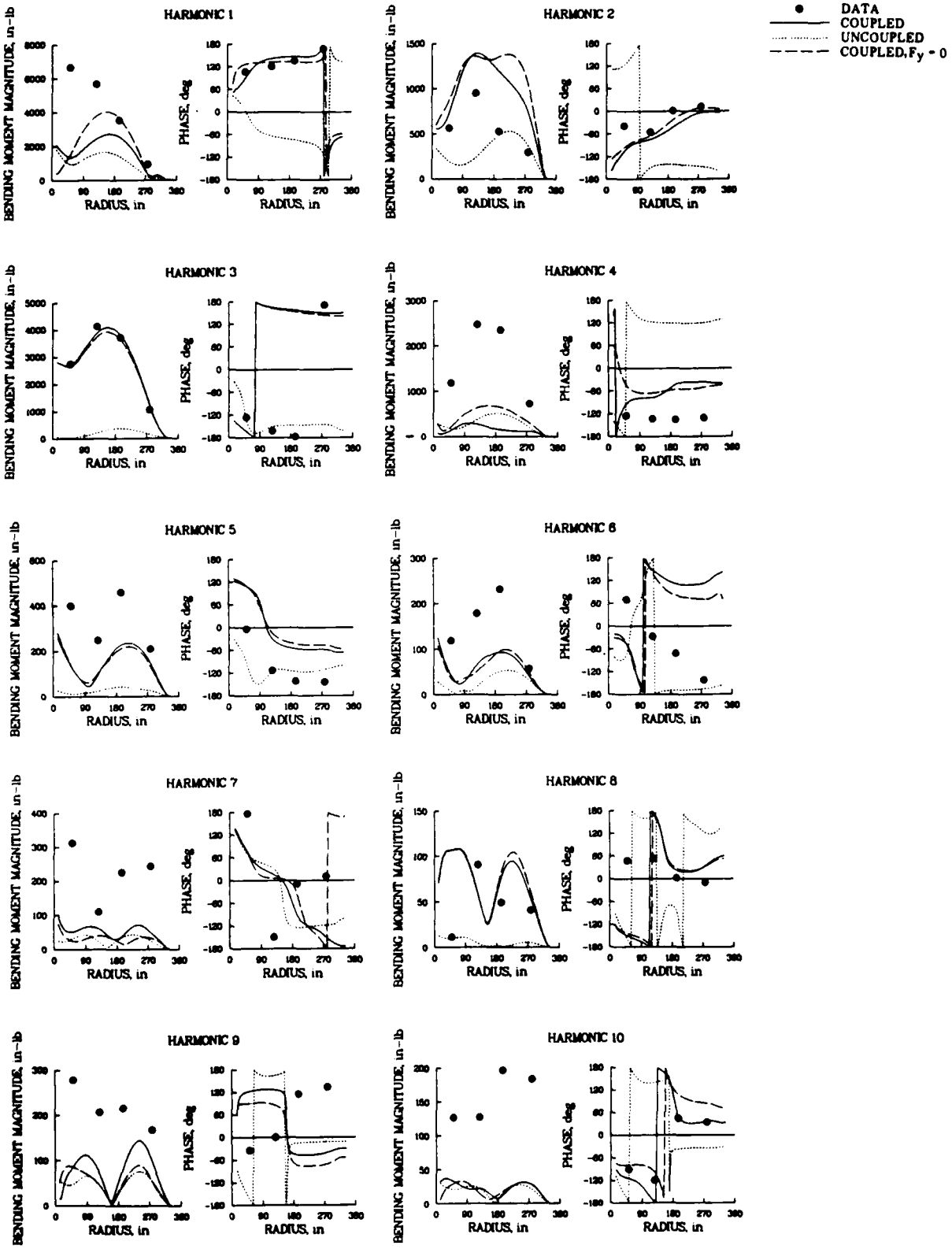

Figure 16. Harmonics of chord-bending moment as a function of radius; flight test, V = 112 knots, rotor speed = 216 rpm.

Lead-Lag Damper Representation. The lead-lag damper that is used on the CH-34 is a hydraulic damper whose force is a nonlinear function of the velocity at the damper. For the calculations shown here, the damper is modeled as a moment boundary condition at the root of the blade, and its force is assumed to be linearly proportional to the velocity at the damper. How sensitive the calculation is to the assumed value of the damper force is an important question, particularly considering the generally poor agreement between the measurements and the calculation for the 1st harmonic of the chord-bending moment. In Fig. 17 the chord-bending moment measurements are compared to the coupled calculations using four different values of the hydraulic-damper damping rate. For the 1st harmonic the effect of increasing the damping rate is to increase the moment on the inboard section of the blade, but in the process there is a moment reversal that is shown in Fig. 17 as a phase reversal. This behavior is very different from the measurements, and it is clear that variation in the damping rate does not explain the lack of agreement for the 1st harmonic. For the 2nd harmonic a damping rate of zero shows the best agreement with the measurements, but in no case is the agreement in phase really satisfactory. For the 3rd harmonic good agreement is achieved in both amplitude and phase using a damping rate of 300 lb-sec/in.; clearly, this harmonic of loading is very sensitive to the assumed value of the damping rate. For the 4th harmonic, the best results are achieved for the higher damping force, but, as in the case of the 2nd harmonic, there is a significant disagreement in phase.

A damping rate of 300 lb-sec/in. has been used for the majority of the calculations in this paper. Figure 18 compares this value of the damping rate (shown as a dashed line) with the measured force characteristics of the damper and a damper velocity histogram. At low velocities, the damping force rises very rapidly to about 1700 lb and then levels off. The initial rate varies from about 800 to 3000 lb-sec/in., while the final rate at high velocities is less than 100 lb-sec/in. The velocity histogram shows the percentage of a cycle where the calculated velocity lies between the indicated velocity values. approximately 60% of one cycle is past the knee of the curve in the low damping region, while the other 40% is in the region of high damping. If the damping rate is increased to 1500 lb-sec/in., the peak velocities are reduced, but the percentage of the time spent in the high and low damping areas does not change. It is clear that any linear approximation of this characteristic cannot expect to be a highly accurate representation of the damper force. The value of 300 lb-sec/in. that is used here is believed to be the best compromise.

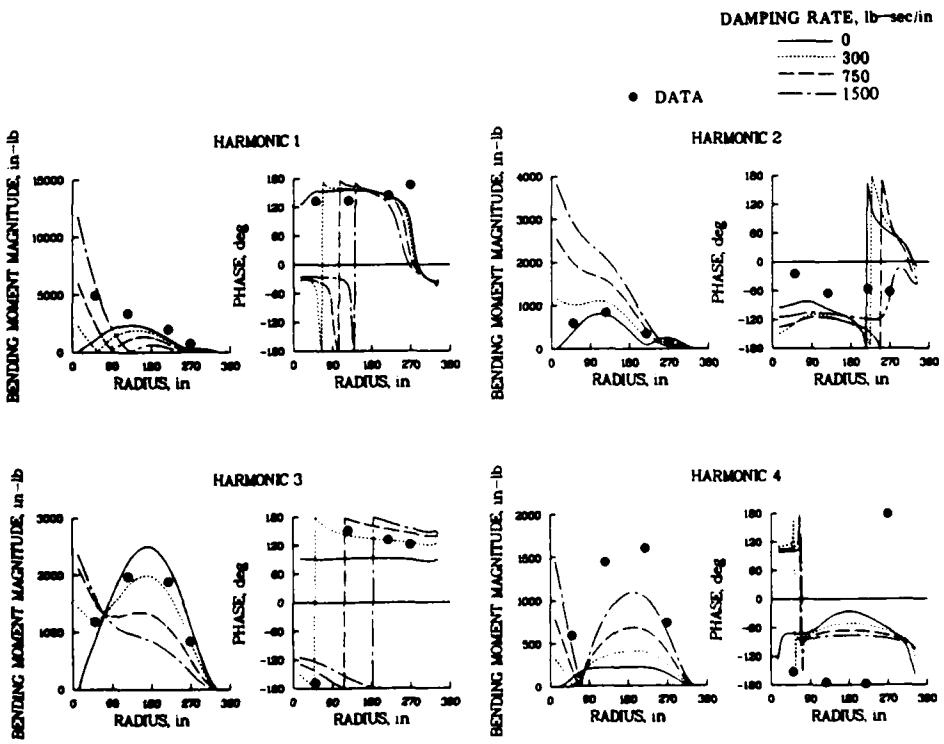

Figure 17. Effect of damping rate on first four harmonics of chord-bending moment.

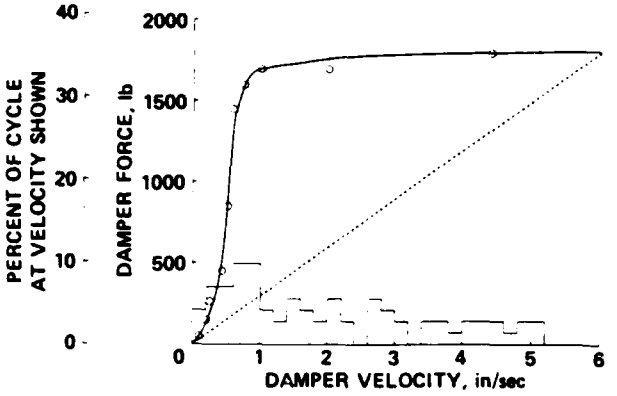

Figure 18. Calculated damper velocity histogram; linear damping rate of 300 lb-sec/in. shown as dashed line.

3/rev Blade Loads. The wind tunnel case shown in Fig. 13 and the flight-test case shown in Fig. 15 are not directly comparable because of the higher airspeed of the wind tunnel case. Despite this airspeed difference, the flight test shows a considerably higher 3/rev loading. The wind tunnel case that is most directly comparable with the flight-test data shown was run at 110 knots with a -9° shaft angle and lift suitable for 1 g flight. The 3/rev loads for these two cases are compared in Fig. 19. Although not shown here the 1/rev loads for these two cases are very similar, but the 3/rev loads measured in flight are twice that obtained in the wind tunnel. It is possible that the difference between the two cases is caused by the different hub impedance between the aircraft and the wind tunnel. In this respect, it is interesting to note that the calculation of the chord-bending moment is quite good for both the wind tunnel and flight conditions, while the calculation of the flap-bending moment in flight

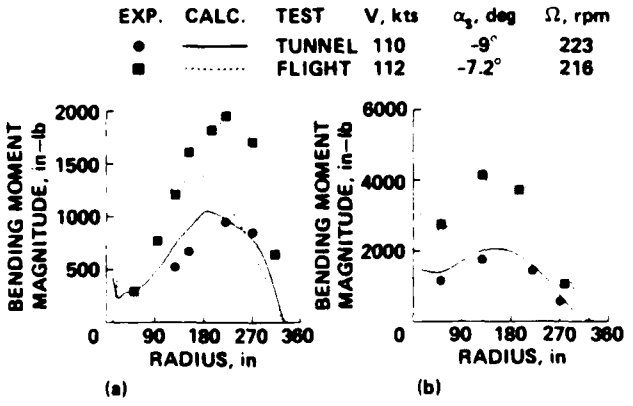

Figure 19. Comparison of 3/rev loading for flight and wind tunnel test cases. a) Flap-bending moment. b) Chord-bending moment.

shows less agreement. The present calculations assume that the rotor hub is fixed, so that any effect of hub motion on blade acceleration is not accounted for. However, any aerodynamic loads caused by hub motion will be lumped into the measured aerodynamics, and will be reflected in the calculations here. If the difference seen here is caused by differences in the hub impedance, the calculations shown in Fig. 19 suggest that the major effect of hub impedance on the chord-vibratory loads is caused by the effects of the hub motion on the airloads. It does not appear that this is the case for the flap-vibratory loads.

If the differences that are seen here are not a result of differences in hub impedance between the flight and wind tunnel tests, this then suggests that the vibratory loads, especially in the chord direction, are very sensitive to small differences in operating conditions between the two tests or differences in the inflow aerodynamics caused by the different fuselage configurations. If this alternative explanation is correct, future CFD models for the calculation of vibratory loads will have to include an accurate solution of the external flow field, including the influence of the aircraft body.

Adequacy of Calculation of Chord-Bending Moment. In general, the agreement between the calculated and measured chord-bending moments is not very good, with the exception of the 3/rev loads. This result is in striking contrast to the agreement seen for the flap-bending moments. The two major uncertainties in the chord-bending-moment calculation are the chord airloads, and the damper representation. As there is no direct measurement of the chord airloads, it is difficult to verify the assumptions used in deriving the chord airloads from the normal airloads. Concerning the lead-lag damper, its characteristics are known to be highly nonlinear and, within the limitations of linear theory, changes in the damper do not have a major impact on the agreement. The representation of the nonlinear damper remains a significant problem.

A number of measurements that were not obtained in the two tests reported on here would be invaluable in any future program. First, it is important to know the actual force characteristics at the lead-lag damper. Secondly, the hub impedances of the aircraft or test stand should be obtained for any future test.

Torsional Moment

Comparison with Wind Tunnel Data. The calculation of the torsional moment is based upon the uncoupled torsion equation. As with the

calculation of the flap-bending moment, there is a direct measure of the aerodynamic forcing terms. However, one difference from the flap-bending moment calculation is the difference in the root boundary condition. For flapping, the moment about the hinge is zero, but for torsion, it is necessary to consider the effect of the control system. For the wind tunnel calculations, a displacement boundary condition was used; the cyclic pitch angles for the first harmonic and a zero displacement angle for the higher harmonics. Figure 20 compares the calculations and measurements for the torsional moment for the 150 knot, -5° shaft-angle case. The calculation agrees very well with the measurements except for an excessive response at 7/rev. This can be seen in the second pair of figures, which shows the comparison for the harmonics 0 to 6. The calculation reproduces the torsional moments that are seen near the blade tip on the advancing side as well as the inboard torsional moments that are caused by reverse flow on the retreating side. The excessive response that is calculated at 7/rev is a result of the blade's 1st torsional mode that is calculated to be at 7.4/rev, and the influence of the displacement boundary condition as will be discussed below.

Comparison with Flight-Test Data. The calculations and measurements for the torsional moment are compared for the 112 knot, 216 rpm case in Fig. 21. For the calculations shown here, a moment boundary condition based upon the measured pitch-link loads was used instead of the displacement boundary condition. The effect of the moment boundary condition is to suppress the 7/rev response, but enhance higher harmonic responses. As in the wind tunnel case, the major torsional moment behavior is accurately reproduced for harmonics 0 to 6, as shown by the lower pair of figures.

The significant effect of the boundary condition on the calculation of the torsional moment is seen in more detail in Fig. 22. Up to the 5th

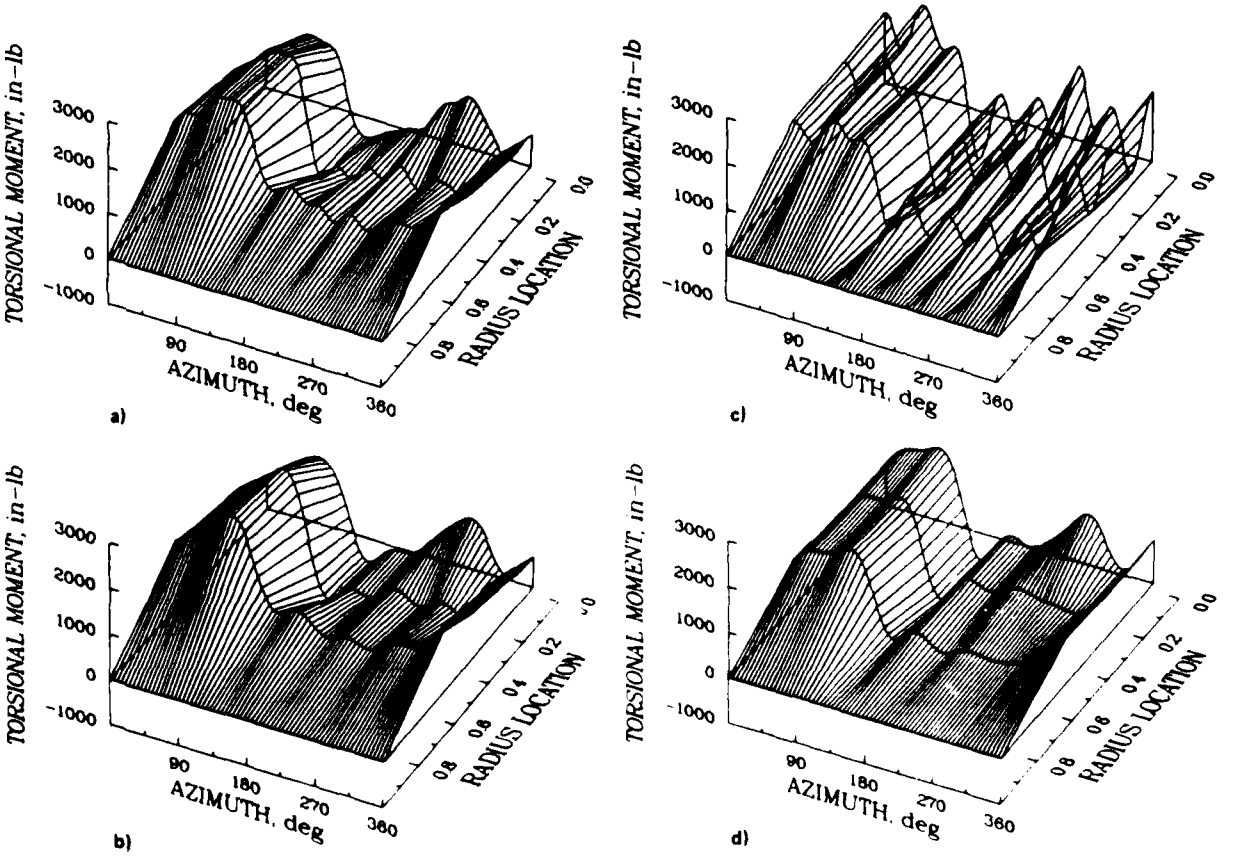

Figure 20. Calculated and measured torsional moments; wind tunnel test, V = 150 knots, shaft angle = -5°. a) Measured torsional moment, 0-10 harmonics. b) Measured torsional moment, 0-6 harmonics. c) Calculated torsional moment, 0-10 harmonics. d) Calculated torsional moment, 0-6 harmonics.

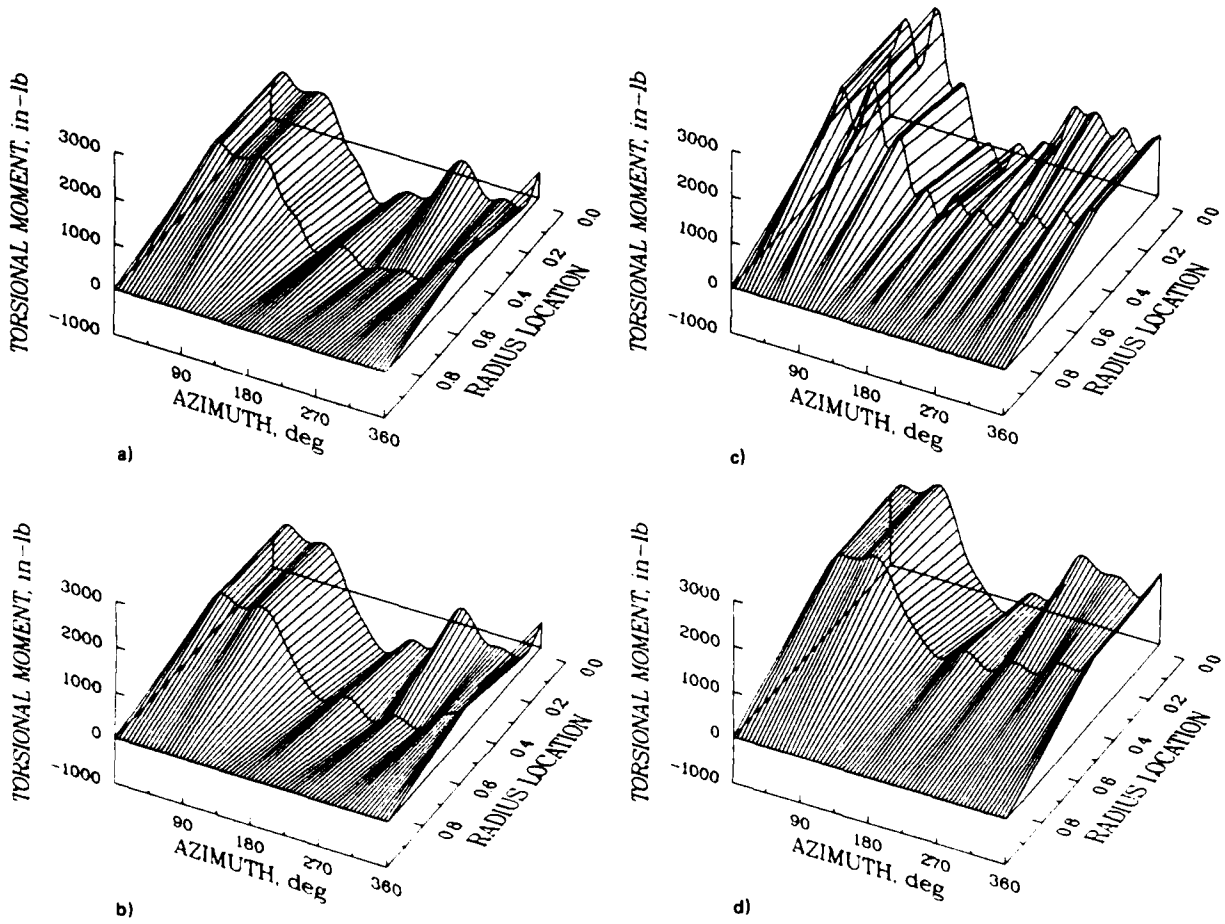

Figure 21. Calculated and measured torsional moments; flight test, V = 112 knots, rotor speed = 216 rpm. a) Measured torsional moment, 0-10 harmonics. b) Measured torsional moment, 0-6 harmonics. c) Calculated torsional moment, 0-10 harmonics. d) Calculated torsional moment, 0-6 harmonics.

harmonic, the two boundary conditions show very similar results. For the 6th through 8th harmonics, the calculated torsional moment is substantially overpredicted using the displacement boundary condition; at higher harmonics, the calculation using the moment boundary condition substantially overpredicts the torsional moment. The sensitivity of the calculation to the boundary condition indicates that the coupling of the blade torsional motions with the control system is important for the accurate calculation of the torsional moment and vibratory loads.

Adequacy of Calculation of Torsional Moment. Comparison of calculation and measurement for the torsional moment shows that the calculation is accurate up to the 6th harmonic for both the wind tunnel and flight-test data. Above the 6th harmonic, the calculation is very sensitive to the assumed boundary condition, that is, whether the displacement is assumed to be zero, which implies that the control system is infinitely rigid, or whether a moment boundary condition is assumed that represents the measured loads in the control system.

The comparison shown here for the 0 to 6 harmonics represents two sets of independent measurement of the aerodynamic pitching moment. As with the flap-bending moment, the good agreement that is seen between the calculation and measurement represents a mutual validation of the accuracy of the two sets of measurements--the differential pressures and the torsional moments.

The sensitivity of the calculations to the boundary condition suggests that in future test programs the impedance or dynamic characteristics of the control system should be measured. In addition, the forces at the pitch-link should be recorded for all test conditions.

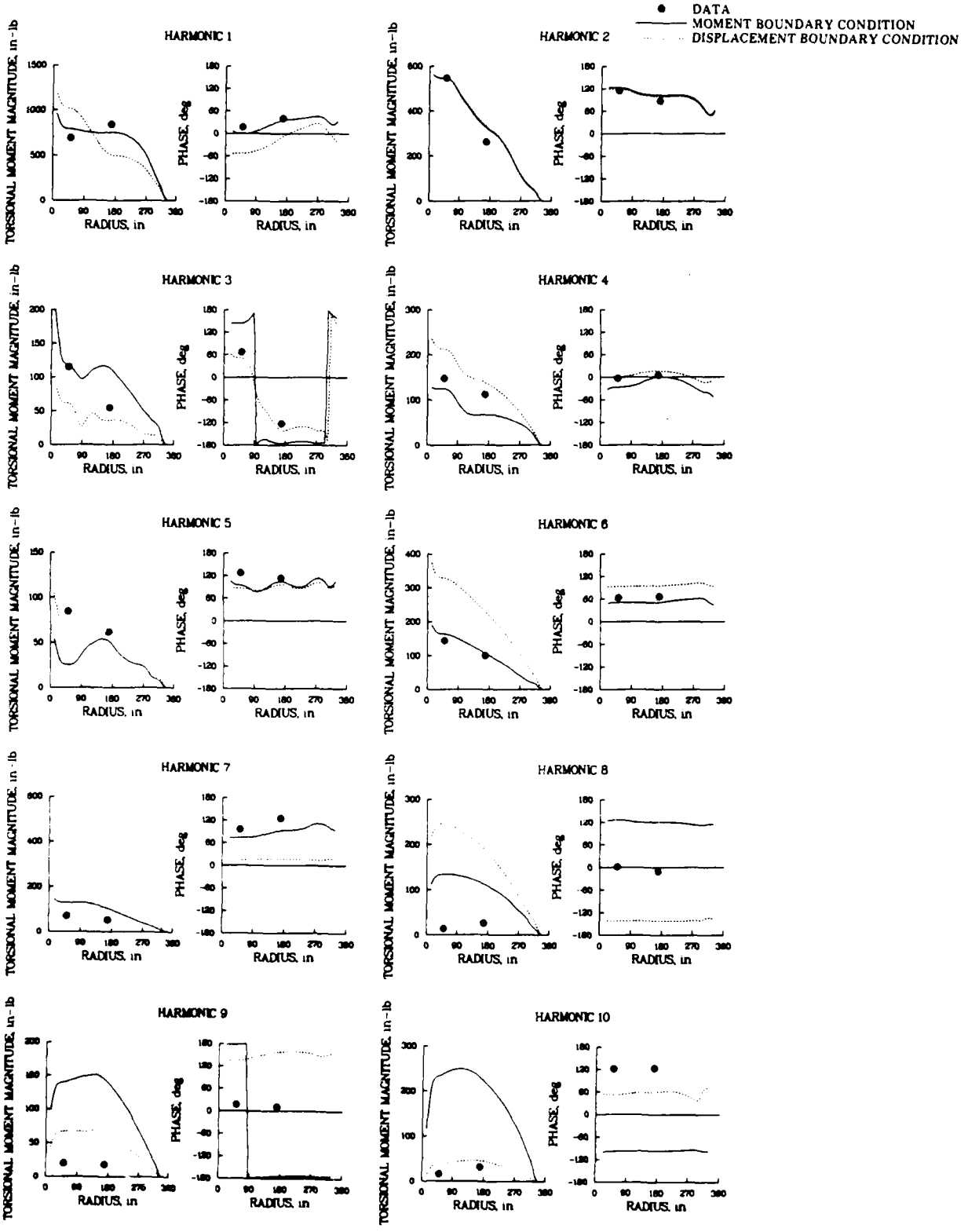

Figure 22. Harmonics of torsional moment as a function of radius; flight test, V = 112 knots, rotor speed = 216 rpm.

Conclusions

The study of the restricted problem of comparing the measured response of a full-scale rotor blade to the calculated response based upon measured airloads results in conclusions in three different areas. First, the comparison of the measured and calculated results allows an assessment of the validity of the structural representation of a rotor blade separate from the aerodynamic model and, where difficulties are identified, emphasizes additional work that is needed. Secondly, the calculations based upon the measurement of differential pressures and the measurements of blade response using strain gages represent two independent sets of measurements, and their agreement or disagreement represents mutual or self-validation of the data. Lastly, measurements that were missing in the data sources used here have caused a number of difficulties which can be avoided in future tests through additional instrumentation, or other improvements.

Comparison of Measurements and Calculation

A comparison of calculations based upon measured airloads and measurement of blade-bending moments results in a number of conclusions:

1) In general, for both the wind tunnel and flight tests, the agreement between the calculated flap-bending and torsional moments and the measured moments is very good. The agreement between calculations and measurements for the chord-bending moments is not good.

2) The comparison of calculation and measurement for the flap-bending moments is better at the lower harmonics where the amplitude is large, than the higher harmonics where the amplitude is small. This is especially noticeable for the flight-test data where it is suspected that the process of digitization from oscillograph records introduced unavoidable errors at higher harmonics. For the wind tunnel data, the amplitudes were not predicted well at the 5th and 8th harmonics, which from calculation are very close or coincident to the 3rd and 4th flap-bending modes. It appears that with an accurate model of the airloads, there should be no difficulty in accurately calculating the flap-vibratory airloads for a rotor system that is as structurally simple to analyze as the one studied here.

3) The reason for the lack of agreement that is seen between the calculated and measured chord-bending moments is unknown. The derivation of the chord airloads and the representation of the lead-lag damper both have a significant impact upon the calculation of the bending-moment response, and the calculations made here were unable to determine the major contributor to the problem. Highly nonlinear dampers of one form or another will be used on most new aircraft for the foreseeable future, and from the results shown here, it appears that it may be difficult to accurately calculate the vibratory inplane loads even with an accurate model of the rotor aerodynamics.

4) The calculation for the torsional moment is better at the lower harmonics than the higher harmonics. The higher harmonic loads are sensitive to the boundary condition at the blade root, and this suggests that coupling with the control system is important for the correct calculation of the torsional moment and pitch-link loads. It appears that with a correct aerodynamic model, there should be no difficulty in accurately calculating the vibratory torsion loads if the control-system stiffness is properly represented for a rotor similar to the one investigated here.

In making these conclusions, it is important to emphasize that the rotor system studied here is relatively simple; that is, the blade degrees of freedom are not strongly coupled and, except for the chord degree of freedom, the boundary conditions are relatively straightforward. This is not the case for a number of present-day rotors whose increased blade twist, tip sweep, and radial nonuniformities in mass and stiffness will increasingly couple the blade motions. In addition, the boundary conditions will be significantly changed for new rotor designs of the hingeless or bearingless type.

Self-Validation of Measurements

The calculations and measurements shown here represent two separate and independent measurements. The calculations are based on the integrated differential pressures measured on the blade, while the measured moment data are from strain-gage measurements. To obtain good agreement between the calculations and measurements of the flap-bending and torsional moments it is necessary that both sets of measurements be obtained accurately, the structural properties be correctly calculated, and the equations of motion used be correct. The good agreement demonstrated here indicates that each of these necessary conditions has been met, and the two sets of measurements validate each other.

Future Test Programs

The comparison of calculated and measured moments reveals a number of problems where the lack of test data has made it difficult to determine the source of differences that have been observed. Additional instrumentation and measurements or different test procedures are needed for any future program to acquire full-scale rotor

pressure and strain data. Such a test should include:

1) Force measurements on lead-lag dampers.

2) Force measurements on pitch-links.

3) Nonrotating shake tests to measure the modal frequencies of the rotor blades.

4) Impedance tests of the control system.

5) Impedance tests of the rotor hub or test stand.

6) Measurement of flap and chord bending moment at a minimum of 10 stations and measurement of torsional moment at a minimum of 6 stations.

7) Rotor speed sweeps in forward flight to allow better identification of the rotating modal frequencies in flight and to determine the sensitivity of the rotor blade moments to rotor speed.

Appendix

The response equation for flap and chord bending for each harmonic is of the form

$$X_n' = AX_n + F_n \tag{10}$$

The original fourth-order equations have been reduced to eight first-order equations in the variables for displacement, slope, bending moment, and shear for the flap and chord degrees of freedom. Coupling between the cosine and sine harmonics because of the structural damping results in a 16-element state vector and a 16 by 16 matrix. The state and force vectors are respectively

$$X_n = \begin{Bmatrix} w_{nc} \\ \psi_{1n} \\ M_{y1n} \\ -V_{z1n} \\ v_{nc} \\ \gamma_{1n} \\ M_{z1n} \\ -V_{y1n} \\ w_{ns} \\ \psi_{2n} \\ M_{y2n} \\ -V_{z2n} \\ v_{ns} \\ \gamma_{2n} \\ M_{z2n} \\ -V_{y2n} \end{Bmatrix} \tag{11}$$

$$F_n = \begin{Bmatrix} 0 \\ 0 \\ 0 \\ F_{znc} \\ 0 \\ 0 \\ 0 \\ F_{ync} \\ 0 \\ 0 \\ 0 \\ F_{zns} \\ 0 \\ 0 \\ 0 \\ F_{yns} \end{Bmatrix} \tag{12}$$

where

$$\begin{aligned} \psi_{1n} &= \psi_{nc} + \gamma\psi_{ns}, & \psi_{2n} &= \psi_{ns} - \gamma\psi_{nc} \\ M_{y1n} &= M_{ync} + \gamma M_{yns}, & M_{y2n} &= M_{yns} - \gamma M_{ync} \\ V_{z1n} &= V_{znc} + \gamma V_{zns}, & V_{z2n} &= V_{zns} - \gamma V_{znc} \\ \gamma_{1n} &= \gamma_{nc} + \gamma\gamma_{ns}, & \gamma_{2n} &= \gamma_{ns} - \gamma\gamma_{nc} \\ M_{z1n} &= M_{znc} + \gamma M_{zns}, & M_{z2n} &= M_{zns} - \gamma M_{znc} \\ V_{y1n} &= V_{ync} + \gamma V_{yns}, & V_{y2n} &= V_{yns} - \gamma V_{ync} \end{aligned} \tag{13}$$

The matrix A is sparse. The nonzero elements are:

$$A_{1,2} = A_{5,6} = A_{9,10} = A_{13,14} = \frac{1}{1+\gamma^2}$$

$$A_{1,10} = A_{5,14} = -A_{9,2} = -A_{13,6} = -\frac{\gamma}{1+\gamma^2}$$

$$A_{6,7} = A_{14,15} = \frac{C_1}{D}$$

$$A_{2,7} = A_{6,3} = A_{10,15} = A_{14,11} = -\frac{C_2}{D}$$

$$A_{2,3} = A_{10,11} = \frac{C_3}{D} \qquad (14)$$

$$A_{3,2} = A_{7,6} = A_{11,10} = A_{15,14} = T$$

$$A_{3,4} = A_{7,8} = A_{11,12} = A_{15,16} = 1$$

$$A_{4,1} = A_{12,9} = m(n\Omega)^2$$

$$A_{8,5} = A_{16,13} = m(\Omega^2 + n^2\Omega^2)$$

$$A_{8,13} = A_{16,5} = m\gamma\Omega^2$$

where

$$C_1 = EI_1 \cos^2\beta + EI_2 \sin^2\beta$$

$$C_2 = (EI_2 - EI_1)\sin\beta\cos\beta \qquad (15)$$

$$C_3 = EI_1 \sin^2\beta + EI_2 \cos^2\beta$$

$$D = C_1C_3 - C_2^2$$

The response equation for torsion for each harmonic is of the form:

$$Y_n' = BY_n + M_n \qquad (16)$$

The original second-order equation has been reduced to two first-order equations in the variables for the torsion angle and bending moment. Coupling between the cosine and sine harmonics because of the structural damping results in a four-element state vector and a 4 by 4 matrix. The state and moment vectors are respectively

$$Y_n = \begin{Bmatrix} \phi_{nc} \\ M_{xn1} \\ \phi_{ns} \\ M_{xn2} \end{Bmatrix} \qquad (17)$$

$$M_n = \begin{Bmatrix} 0 \\ M_{nc} \\ 0 \\ M_{ns} \end{Bmatrix} \qquad (18)$$

where

$$M_{xn1} = M_{xnc} + \gamma M_{xns}, \quad M_{xn2} = M_{xns} - \gamma M_{xnc} \qquad (19)$$

The nonzero elements of the matrix B are:

$$B_{1,2} = B_{3,4} = \frac{1}{(1+\gamma^2)}\frac{1}{GJ}$$

$$B_{1,4} = -B_{3,2} = -\frac{\gamma}{(1+\gamma^2)}\frac{1}{GJ} \qquad (20)$$

$$B_{2,1} = B_{4,3} = m\Omega^2(k_{m2}^2 - k_{m1}^2) - mk_m^2\omega^2$$

$$B_{2,3} = -B_{4,1} = m\Omega^2\gamma(k_{m2}^2 - k_{m1}^2)$$

and $k_{m2}^2 = k_m^2$ and $k_{m1}^2 = 0$ because the airfoil is thin.

Acknowledgment

The work reported here was done under the auspices of the Memorandum of Understanding between France and the United States for Cooperative Research in Helicopter Dynamics.

Mr. Wen-Liu Miao of Sikorsky Aircraft is acknowledged for his assistance in obtaining reference material on the CH-34 rotor.

References

[1]Ormiston, Robert A., "Comparison of Several Methods for Predicting Loads on a Hypothetical Rotor," Proceeding of the AHS/NASA Ames Specialist' Meeting on Rotorcraft Dynamics, NASA SP 352, Feb. 1974, pp. 284-302.

[2]Sweers, J. E., "Theoretical Prediction of Airloads and Structural Loads and Correlation with Flight Test Measurements," USAAVLABS TR 68-22C, May 1968.

[3]Hooper, W. E., "The Vibratory Airloading of Helicopter Rotors," Paper No. 46, Ninth European Rotorcraft Forum, Sept. 1983, Stresa, Italy.

[4]Scheiman, James, "A Tabulation of Helicopter Rotor-Blade Differential Pressures, Stresses, and Motions as Measured in Flight," NASA TM X-952, Mar. 1964.

[5]Rabbott, J. P., Jr., Lizak, A. A., and Paglino, V. M., "A Presentation of Measured and Calculated Full-Scale Rotor Blade Aerodynamic and Structural Loads," USAAVLABS TR 66-31, July 1966.

[6]Rabbott, J. P., Jr., Lizak, A. A., and Paglino, V. M., "Tabulated CH-34 Blade Surface Pressures Measured at NASA/Ames Full Scale Wind Tunnel," SER-58399, Dec. 1965.

[7]Niebanck, Charles F., "Model Rotor Test Data for Verification of Blade Response and Rotor Performance Calculations," USSAMRDL-TR-74-29, May 1974.

[8]McHugh, Frank J., "What Are the Lift and Propulsive Force Limits at High Speed for the Conventional Rotor?" American Helicopter Society 34th Annual National Forum, Washington, D.C., May 1978.

[9]Houbolt, John C. and Brooks, George W., "Differential Equations of Motion for Combined Flapwise Bending, Chordwise Bending, and Torsion of Twisted Nonuniform Rotor Blades," NACA Report 1346, 1958.

[10]Murthy, V. R., "Dynamic Characteristics of Rotor Blades," Journal of Sound and Vibration, Vol. 49, No. 4, Dec. 1976, pp. 483-500.

[11]Meirovitch, Leonard, Analytical Methods in Vibrations, The Macmillan Company, 1967.

[12]Coleman, R. P., Feingold, A. M., and Stempin, C. W., "Evaluation of the Induced-Velocity Field of an Idealized Helicopter Rotor," NACA ARR L5E10, June 1945.

[13]Rice, John R., Numerical Methods, Software, and Analysis: IMSL(R) Reference Edition, McGraw-Hill Book Company, 1983.